# Dynamic Testing of Permanent Magnet Synchronous Machines

**Sebastian Hall**

LUND UNIVERSITY

**Licentiate thesis**
**Division of Industrial Electrical Engineering and Automation**
**Department of Biomedical Engineering**

**2016**

Division of Industrial Electrical Engineering and Automation
Department of Biomedical Engineering
Faculty of Engineering
Lund University
Box 118
221 00 Lund
SWEDEN

http://www.iea.lth.se

ISBN: 978-91-88934-68-0
CODEN: LUTEDX/TEIE-1076/1-134/(2016)


Printed in Sweden by Tryckeriet i E-huset
Lund 2016

This too shall pass

*(Anna P)*

# Acknowledgements

The first thank you goes out to Professor Alaküla for realizing this project. The support and motivational talks have been phenomenal. The second thank you is for Associate Professor Reinap for the availability and philosophical perspective on engineering and life. Fantastic. My research group crew definitely deserves a big salute for the helpful discussions. Then of course, I cannot forget to mention the one and only Getachew Darge, king of the workshop, savior of the day. Also, Carina and Ulrika, the queens of administration, have my sincerest gratitude for saving me on several occasions. Actually, thanks to the whole division of Industrial Electrical Engineering and Automation. I am sorry if I missed a coffee week; if so, it was not on purpose. Finally, I must give credit to the ELDRIVET group for the support and interesting get-togethers.

Outside of work I thank my family and friends for putting up with occasional whining due to motivational downswings. You are the best and I would probably pass away in an instance if you went away. **Tack!**

# Abstract

This thesis presents a method to test and characterize Permanent Magnet Synchronous Machines (PMSMs) called the Dynamic Test Method (DTM). In contrast to traditional methods, the DTM tests machines without a brake or a locking mechanism for the test object's rotor. Instead, the moment of inertia of the rotor shaft limits the mechanical dynamics while a voltage source imposes torque producing currents on the stator windings of the machine. While a specific predefined current produces a torque which accelerates and brakes the machine, a data acquisition system samples measurements of the phase currents, the phase voltages and the rotor position with a high sampling frequency. A post-processing algorithm then derives the performance of the machine for the specific phase currents from the sampled data.

The main focus of this work lies on the magnetic model identification. The magnetic model describes the relationship between the currents and the linked magnetic flux in a machine. The model gives feedback to designers, provides the air-gap torque characteristics of the machine and helps with the implementation of optimal field-weakening control. Through equations from the equivalent model of the PMSM, the obtained data yields the linked magnetic flux as a function of the test currents. The method derives the flux from measurements from both the motor and the generator regime of the machine, and can therefore obtain the flux without knowledge of the stator winding resistance. This also makes it possible to disregard the iron losses influence on the flux linkage. Experimental results show a good match between the DTM test results and results from a traditional constant speed method. The experiments show that the temperature has little effect on the DTM results compared to the constant speed method.

The DTM also provides the torque characteristics of a PMSM. The method derives the air-gap torque from the linked magnetic flux and currents, and also the rotor shaft torque from the acceleration and moment of inertia. To derive the rotor shaft torque, this work presents a method to obtain the rotor shaft moment of inertia from a pendulum and flywheels. Experimental measurement results from both the motor and generation operation show good consistency of the torque measurements. Furthermore, the average values between the generator and motor tests show that the moment of inertia of the rotor shaft can be obtained solely from the dynamic tests. This makes it possible to derive the efficiency and losses of the machine without a torque sensor or knowledge about the moment of inertia of the rotor shaft.

In addition to the magnetic model identification and the torque performance characterization, this thesis also outlines a theoretical framework for efficiency derivation and loss separation of a test object. The efficiency tests provide a fast evaluation of the machine which can compliment the more detailed tests in a conventional test setup. The method derives the efficiency from the electric power, which it calculates from the voltages and currents, and the mechanical power, which is calculated from the acceleration, speed and moment of inertia of the rotor shaft. Experimental tests show that there still exist question marks regarding the performance of the method. The rotational speed of the test object does not reach the expected, and the efficiency results are low. Even so, the results give a steady foundation for future research.

# Nomenclature

| | |
|---|---|
| $\alpha$ | Bandwidth of PI controller |
| $\alpha_e$ | Voltage error factor |
| $\beta$ | Converter semi-conductor voltage drop error factor |
| $\cos(\phi)$ | Power factor |
| $\delta$ | State of a converter leg |
| $\eta$ | Efficiency |
| $\omega_{\text{ex}}$ | Resolver excitation frequency |
| $\omega_{\max}(i_d^s, i_q^s)$ | Maximum speed for a specific current combination in the $dq$ frame |
| $\omega_b$ | Cut-off frequency for the moving average filter |
| $\omega_m$ | Rotor shaft rotational frequency |
| $\psi_m$ | Linked permanent magnet flux |
| $\Psi_{dq}^s(s)$ | $dq$ linked flux vector in the frequency domain |

$\psi_{dq}^{\left(i_d^{\psi}, i_q^{\psi}\right)}$ Linked magnetic flux in the $dq$ frame

$\psi_{dq}^{\left(i_d^{s}, i_q^{s}\right)}$ Mean value of the linked flux from the motor and the generator region

$\theta$ Rotor angular position

$\theta_{dq}^{i}$ $dq$ current vector angle in respect to the $d$ axis

$\theta_{dq}^{u}$ $dq$ voltage vector angle in respect to the $d$ axis

$\vec{\psi_{dq}^{s}}$ $dq$ linked magnetic flux vector in polar coordinates

$\vec{i_{dq}^{s}}$ $dq$ current vector in polar coordinates

$\vec{u_{dq}^{s}}$ $dq$ voltage vector in polar coordinates

$c_i$ Integral gain for the Direct Current Control algorithm

$i_{dq}^{\psi}$ Equivalent current which gives rise to linked flux

$i_{dq}^{f}$ Equivalent iron loss current in the $dq$ frame

$i_{dq}^{s}$ Stator winding currents in the $dq$ frame

$I_{dq}^{s}(s)$ $dq$ current vector in the frequency domain

$J$ Rotor shaft moment of inertia

$J_f$ Fly-wheel moment of inertia

| | |
|---|---|
| $J_p$ | Pendulum moment of inertia |
| $k$ | Transformation scaling factor |
| $K_e$ | Eddy current loss coefficient |
| $K_f$ | Mechanical friction coefficient |
| $K_h$ | Hysteresis loss coefficient |
| $k_i$ | PI controller integral gain |
| $k_p$ | PI controller proportional gain |
| $K_{exc}$ | Excess loss coefficient |
| $L$ | Stator winding inductance (Varies with the rotor position) |
| $p$ | Number of pole pairs |
| $P_m$ | Mechanical power |
| $P_e$ | Electric power |
| $R_f$ | Equivalent eddy current loss resistance |
| $R_s$ | Stator winding resistance |
| $T_{ag}^m$ | Mean air-gap torque from the motor and the generator regime |
| $T^{ext}$ | External rotor shaft torque |
| $T_{loss}^{mec}$ | Mechanical loss torque |

$T_{ag}$ Air-gap torque

$T_{loss}$ Torque due to iron losses and mechanical losses

$T_{rs}$ Rotor shaft torque

$u_d^{\text{res}}$ The direct resolver signal

$u_q^{\text{res}}$ The quadrature resolver signal

$u_{\text{abc}}$ Phase voltages

$U_N$ Voltage from converter phase leg to DC-link minus

$U_n$ Voltage from converter phase leg to machine neutral

$u_{\alpha\beta}$ Voltage in the $\alpha\beta$ frame

$U_{dc}$ DC-link voltage

$u_{dq}$ Voltage in the $dq$ frame

$U_{dq}^s(s)$ $dq$ voltage vector in the frequency domain

$U_{drop}$ Voltage drop over semi-conductor components in the converter

# List of Figures

# List of Tables

# Contents

# Chapter 1

# Introduction

The dynamic testing method (DTM) project was created to assist the global endeavor to move away from the environmentally unfriendly and insecure fossil-energy dependence. It took part in the bigger venture ELDRIVET, which intended to support the transition from combustion engines to electric drives in the Swedish vehicles fleet. Within ELDRIVET, the DTM project was assigned to develop a test method to facilitate the development, manufacturing and employment of electrical machines in vehicles. Vehicle developers often consider permanent magnets synchronous machines (PMSMs) for traction due to their high performance; therefore, it was decided to focus on these machines.

This thesis presents the outcome of the DTM project. In hindsight, the development has been a success in the sense that the methodology shows a big potential to be useful for the industry. The quickness of the test procedure and the need for little equipment and space makes it optimal for fast characterizations of machines, which can be used as a first feed-back on machine designs or as a performance control for machines in serial production. In addition, the method shows possibilities for increased accuracy with more development. With all this in mind, this work can hopefully play a tiny part in saving the world.

## 1.1 Why dynamic testing?

The concept of testing machines dynamically is not new, and description of such methods can be found in for instance the IEEE standard for testing synchronous machines [1]. Here follows a general outline of the procedures:

1. A drive accelerates a test object to a predefined speed by imposing currents with constant amplitudes on the armature windings.

2. During the acceleration, a data acquisition system reads measurements of the acceleration of the rotor shaft.

3. The acceleration and moment of inertia of the shaft then yield the torque on the rotor as a function of the currents.

While these tests derive the torque characteristics of a machine, the DTM which this thesis presents extends the method to include magnetic model characterization and efficiency property measurements. This subsection compares the DTM to other test methods and argues why the development of new procedures is relevant.

The first part of the subsection discusses the magnetic model derivation. The magnetic model describes the currents relationship to the magnetic flux in the machine. Information about these properties give possibilities to design optimal control algorithms and gives valuable feedback to machine designers. The results also make it possible to estimate the air-gap torque which can be compared to the rotor shaft torque for loss estimation in the machine. The second part discusses efficiency testing. Information about the efficiency and losses is fundamental to perform lifetime estimations and life-cycle cost analysis on machines. Furthermore, the efficiency together with the torque measurements give a direct indication if something is wrong with the machine.

### Magnetic model derivation

The literature presents numerous ways to derive the electromagnetic properties of a PMSM. Different methods are used for different purposes: Simulations can optimize the performance of the machine in an early design state. Supposing the material characteristics of the machine are known, FEM simulations provide accurate information of a machine's characteristics [2], [3]. On-line methods verify machine parameters while the machine is active in its application. Continuously updated information can be used for sensorless control, diagnostics and monitoring of the machine [4], [5], [6].

A third way to evaluate the machine is by off-line experimental tests. The off-line tests provide information for optimal control, machine diagnostics and feed-back on prototype design. They can be divided up into two main categories: Stand-still methods (SSMs) and constant speed methods (SCMs). As the name implies, the SSMs characterizes the machine without motion; the rotor is locked mechanically while different torque producing currents are imposed on the stator windings [7], [8], [9]. The reactions of the phase currents and voltages are then measured, and mathematical expressions derive the relationship between the current and magnetic flux linkage from the obtained data.

Stand-still methods have the drawback of not being able to provide information about the flux linkage from the permanent magnets, and the testing can not be extended to evaluate the efficiency of the machine. Constant speed methods (CSM), on the other hand, can do both of these things. When the CSMs perform the testing, an additional brake machine holds the speed of the test object constant while the clamp voltages are measured; the voltage measurements together with the PMSMs voltage equations then yield the magnetic flux in post-processing calculations. Even though the CSMs can derive all the necessary information about the machine, they require expensive equipment and test facilities. In addition, the time duration of the procedures is usually high, which leads to bad time efficiency and possible heating of the machine, which in turn can lead to distortion in the measurement results.

The drawbacks of the SSM and CSM characterization methods give room for alternative concepts, and one possible test alternative is the DTM. Even though torque producing currents are imposed on the test object with an unlocked rotor, the test procedure does not involve a brake machine. Instead, the machine accelerates while the moment of inertia of the rotor axis limits the acceleration. In the mean while, sensors and a data acquiring system obtain measurements which can derive the linked magnetic flux in post-processing calculations. Theoretically, this methodology takes the best aspects of the SSM and the CSM concepts without losing anything. This, of course, requires that the accuracy of the results are not inferior to the other methods.

### Efficiency testing

In contrast to electrically magnetized synchronous machines, asynchronous machines and DC machines, there exists no standard (which the author know of) which treats PMSMs. With that being said, there still exist documents with guidelines for efficiency testing of PMSMs, and they generally base there recommendations on the standard for testing of synchronous machines [10], [11], [12], [1]. The synchronous machine standard presents two ways to derive the efficiency. In the first method, the input and output power of the machine are measured. The efficiency can be calculated directly from the measurements as

$$\eta = \frac{output}{input} \cdot 100 \tag{1.1}$$

The second method requires that the different losses of the machine are measured first, and the efficiency may then be calculated according to

$$\eta = 100 - \frac{losses \cdot 100}{input} \tag{1.2}$$

for a motor, and

$$\eta = 100 - \frac{losses \cdot 100}{losses + output} \tag{1.3}$$

for a generator; this procedure is called the segregated losses method.

In most common ways to measure the efficiency of a PMSM, an additional test machine drives or brakes the test object throughout the test procedures. A power meter measures the electric output power from the converter while rotor axis torque and speed measurements yield the mechanical power of the machine. The efficiency can then be calculated with the input-output method. If the test machine's loss characteristics are known, speed-dependent losses may be measured from open circuit tests at different frequencies. The resistance can be measured with an impedance meter and the efficiency can then be derived by the segregated loss method. The changed temperature in the test object which the losses induce can also be measured throughout the tests. This requires special facilities with high control of the ambient temperature.

All of these methods demand time and require expensive equipment and facilities. This motivates the development of new concepts for efficiency evaluation of machines. The dynamic test method introduces a method which gives a quick and cheap estimation of the efficiency and losses to complement to the the accurate but time and cost inefficient constant speed tests.

## 1.2 Objectives and Limits

The list below presents an overview of the objectives of this work:

- Extend the theoretical base of the method. Earlier articles from the division of Industrial Electrical Engineering and Automation

(IEA) of Lund University outline the concept [13]. This thesis should give an in depth explanation of the theory behind it.

- Concentrate on the magnetic model derivation and torque characterization part of the DTM. The possibilities of efficiency measurements and loss separation procedures should be discussed and evaluated as far as time and space allows.

- Present an extensive experimental evaluation of the method. Test results should be compared to simulations and data from an established CSM. Discuss eventual deviations in the results.

- Present and discuss data acquisition procedures, post-processing of measurement data and the consequence of measurement errors. Present the methods that were used throughout the experimental tests.

- Discuss strength and weaknesses of the method. Propose topics for future research.

Below follows the limits of the work:

- The measurement considerations part of chapter 2 focuses on the magnetic model identification part of the DTM (but a lot of information there also applies to the efficiency measurements and loss separation).

- The implications of measurement errors presented in chapter 2 are not evaluated with either simulations or experimental tests. An analysis of that kind would indeed be interesting, but is out of the scope of this thesis.

- The loss separation possibility is only partly discussed in this thesis, but is a good topic for future research.

- The theories about why unexpected measurement phenomena occur that chapter 5 presents are not tested by simulations or ex-

perimental tests. Such tests would contribute a lot to the thesis, but due to lack of time they were not performed.

## 1.3 Disposition

The list below gives the reader a quick introduction to the following chapters in this thesis

- Chapter 2 (Theory and Method Description) gives a thorough explanation of the theory behind the different parts of the DTM. It goes through the testing process step by step and points out important considerations along the way. Furthermore, current control strategies which suit the DTM well are presented. The end of the chapter discusses data acquisition considerations, post-processing algorithms and consequences of measurement errors.

- Chapter 3 (Experimental Setup) describes the equipment that was used during the experimental tests. The test object as well as the data acquisition and control system are taken into account for. Furthermore, the chapter describes the additional test bench which the constant speed tests used.

- Chapter 4 (Experimental Results) presents the results from DTM experimental tests. The DTM is compared to a CSM in the magnetic model identification section. The section also evaluates the temperature's influence on the results. Later parts of the chapter present an extensive consistency analysis of the DTM torque characterization. The analysis extends to compare the derived air-gap and rotor-shaft torque. The last parts of the chapter present efficiency and power factor results.

- Chapter 5 (Deeper Analysis of Results) discusses unexpected results from Chapter 4. The flux's and torque's speed dependence is given special attention.

- Finally, the last chapter concludes the thesis with remarks, recommendations and proposals for future work.

## 1.4 Contribution

The main contribution from this work is the extensive evaluation of dynamic testing of PMSMs. It gives the reader an idea of when the method is suitable to use, and under which conditions it is not optimal. Furthermore, it gives suggestions for future research which can help the progress within the field of machine testing and characterization.

## 1.5 Publications

Marquez-Fernandez, F.J. Hall, S. Alaküla, M., "Dynamic testing characterization of a HEV traction motor," in *Electrical Machines (ICEM), 2014 International Conference on* , vol., no., pp.1569-1575, 2-5 Sept. 2014

Hall, S. Loayza, Y. Reinap, A. Alaküla, M., "Consistency analysis of torque measurements performed on a PMSM using dynamic testing," in *Electrical Machines (ICEM), 2014 International Conference on*, vol., no., pp.1529-1535, 2-5 Sept. 2014

Hall, S. Loayza, Y., "An evaluation of two Direct Current Control methods implemented with LabVIEW on a FPGA," in *Electrical Machines and Systems (ICEMS), 2013 International Conference on*, vol., no., pp.1455-1460, 26-29 Oct. 2013

Reinap, A. Alaküla, M. Hall, S. Estenlund, S., "Performance estimation of hybrid excited machine with alternating pole configuration," in *Electrical Machines (ICEM), 2014 International Conference on*, vol., no., pp.2638-2643, 2-5 Sept. 2014

# Chapter 2

# Theory & Method Description

This chapter presents a theoretical overview of the dynamic test method (DTM) together with measurement procedures, data post-processing approaches, and consequences of measurement errors. The permanent magnet synchronous machine (PMSM) model which works as the foundation for the theory of the derivation of magnetic model is adressed in the first part of the chapter (section 2.1). The section explains the process of representing a PMSM in the rotating reference frame ($dq$ frame), and presents a PMSM equivalent circuit in the $dq$ frame.

Section 2.2 presents the DTM magnetic model identification process. The passage goes through the procedure of the experimental testing, and explains the theory behind how the magnetic flux is obtained from the measurements. Section 2.3.2 explains the DTM torque characteristic determination. The part only describes the theory of the data treatment since the post-processing system derives the torque from the same data that is used in the magnet model identification. The DTM machine efficiency derivation is addressed in section 2.4. The section presents the theory of the calculations from the measurements and explains why the measurements from the magnetic model derivation can not be reused. The section also discusses the possibility of expanding the DTM to include loss separation.

The data acquisition process is discussed in the last part of the chapter (section 2.5). The section addresses different methods to obtain the necessary DTM data, and the methods that were used to derive the re-

sults which chapter 4 presents are explained. The passage also provides measurement data post-processing techniques and discusses the results of different measurement errors.

## 2.1 Machine model

To understand the theory behind the derivation of the PMSM magnetic model, an analytical representation of the PMSM which shows the magnetic flux relationship with the stator voltages and currents is necessary. The literature presents numerous variations of analytical PMSM models with varying complexity. In addition to the standard components – the stator winding resistance and inductance, and the induced voltage – models can include iron losses modeled as a parallel resistance [14], a series resistance [15] or as a series voltage source [16]. Furthermore, phenomena such as inductance cross-coupling and cogging torque can be taken into account [17], [18].

The models are often expressed in the $dq$ frame, which represents the oscillating three phase system as constant values in a steady-state situation, as proportional integrator (PI) current controllers usually need constant steady-state reference values to perform well. The $dq$ frame also suits the DTM magnetic model as optimal field-weakening PI control generally needs information about the flux characteristics of the machine. The following sections define the $dq$ frame and present this works PMSM equivalent model.

### 2.1.1 The $dq$ frame

The $dq$ frame is in this thesis defined as a coordinate system which rotates counter clockwise with the electrical frequency, and where the $d$ axis is aligned with the linked magnetic flux from the permanent magnets. To derive the stator voltages and currents in the $dq$ frame, the $\alpha\beta$ matrix first transforms the three phase phasors to two ortigonal

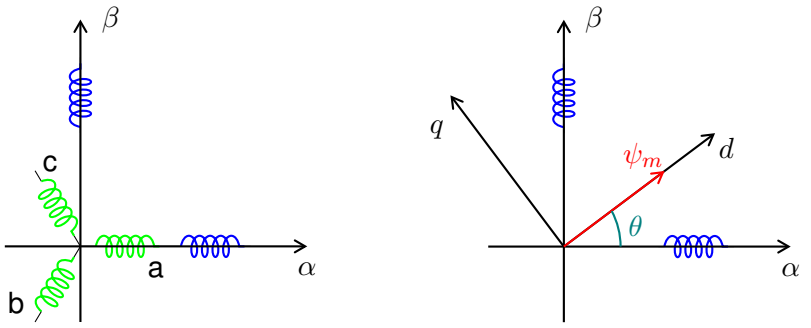


(a) The three phases of a PMSM together with the two phase alpha beta representation

(b) The two phase alpha beta coordinate system together with the rotating $dq$ system

Figure 2.1: Coordinate systems of a PMSM

phasors. Expression (2.1) shows the $\alpha\beta$ matrix, where $K$ is a transformation index which scales the $\alpha$ and $\beta$ phasors. The phasors can for example be scaled to be amplitude invariant ($k = \frac{2}{3}$) or power invariant ($k = \sqrt{\frac{2}{3}}$), but $k$ can be chosen arbitrarily to ones needs. Figure 2.1a shows the relationship between the three phases and the $\alpha, \beta$ axes.

$$\begin{bmatrix} u_\alpha \\ u_\beta \end{bmatrix} = k \begin{bmatrix} 1 & -\frac{1}{2} & -\frac{1}{2} \\ 0 & \frac{\sqrt{3}}{2} & -\frac{\sqrt{3}}{2} \end{bmatrix} \begin{bmatrix} u_a \\ u_b \\ u_c \end{bmatrix} \tag{2.1}$$

To transform the $\alpha, \beta$ coordinates to $dq$ coordinates, the Euler rotational matrix, shown in (2.2), rotates the $\alpha\beta$ axes with the rotor position $\theta$. The rotor position is defined as zero when the $d$ axis is aligned with the $\alpha$ axis (when the permanent magnet flux faces the windings of phase a). Figure 2.1b shows the relationship between the $\alpha\beta$ and the $dq$ reference systems.

$$\begin{bmatrix} u_d \\ u_q \end{bmatrix} = \begin{bmatrix} \cos\theta & \sin\theta \\ -\sin\theta & \cos\theta \end{bmatrix} \begin{bmatrix} u_\alpha \\ u_\beta \end{bmatrix} \tag{2.2}$$

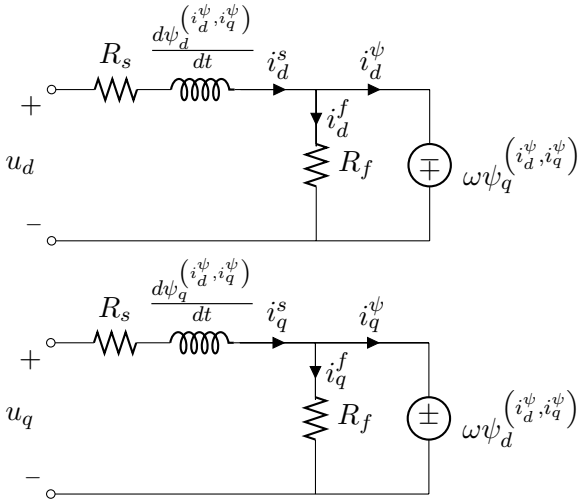


Figure 2.2: Equivalent circuit of the PMSM in the $dq$ reference frame

### 2.1.2 Equivalent circuit

Figure 2.2 shows the equivalent PMSM model of this work. The resistance $R_s$ represents the voltage drop over the stator winding resistance; $\frac{d\psi^{(i_d^\psi, i_q^\psi)}}{dt}$ the voltage drop due to change in the linked magnetic flux in $dq$ coordinates; the parallel resistance $R_f$ the eddy current iron losses in the machine; and the voltage sources represent the induced voltage due to the linked magnetic flux. The iron losses are hard to model due to their nonlinear behavior, and the resistance is mainly included for a conceptual purpose. As is seen in Figure 2.2, part of the measured stator current $i^s$ excites the eddy current losses, which means that not all of the stator current introduces flux linkage. Other phenomena, such as hysteresis losses and excess iron losses also affect the linkage of the magnetic flux, but are left out of the model due to their complexity. The Kirchoff voltage law gives the voltage equations of the equivalent circuit

$$u_d = R_s i_d + \frac{d\psi_d^{\left(i_d^\psi, i_q^\psi\right)}}{dt} - \omega \psi_q^{\left(i_d^\psi, i_q^\psi\right)} \tag{2.3}$$

$$u_q = R_s i_q + \frac{d\psi_q^{\left(i_d^\psi, i_q^\psi\right)}}{dt} + \omega \psi_d^{\left(i_d^\psi, i_q^\psi\right)} \tag{2.4}$$

In the DTM, the control system holds the $dq$ currents constant during one test cycle. The derivative of the $dq$ flux is therefore approximately zero, and $\frac{d\psi^{\left(i_d^\psi, i_q^\psi\right)}}{dt}$ becomes zero (The iron losses make the flux linkage change slightly with increased speed, but considering electrical dynamics the change is negligible). The voltage equations which are relevant for the DTM become

$$u_d = R_s i_d - \omega \psi_q^{\left(i_d^\psi, i_q^\psi\right)} \tag{2.5}$$

$$u_q = R_s i_q + \omega \psi_d^{\left(i_d^\psi, i_q^\psi\right)} \tag{2.6}$$

## 2.2 Magnetic model identification

### 2.2.1 Test procedure

To test a PMSM with the DTM, the test object should be mounted firmly on a stable platform. A fly-wheel is preferably mounted on the machine's rotor axis to slow down the mechanical dynamics when torque is applied. The machine is connected to a variable frequency drive system which supplies the machine with voltage and current. For each current combination in the $dq$ frame which is desirable to evaluate, a test cycle is performed:

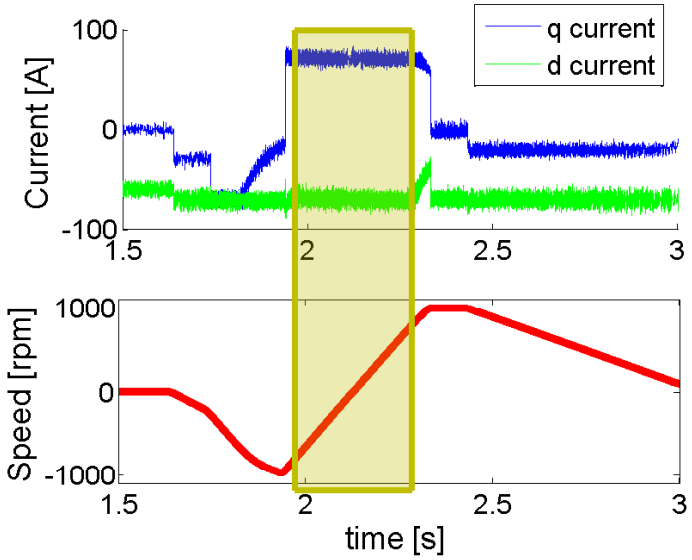


Figure 2.3: Dynamic test sequence for magnetic model derivation

1. A voltage source drive accelerates the machine with a combination of $dq$ currents to a pre-defined negative speed.

2. The drive brakes the machine to stand-still with the same $d$ current and the inverse of the $q$ current from point 1).

3. Maintaining the same current combination, the drive accelerates the machine to the same magnitude of the speed as in point 1 (but with a positive sign).

4. The drive brakes the machine to stand-still.

Notice that the machine works as a generator when it brakes, and the drive system must therefor be able to absorb as well as deliver electrical energy throughout the test sequence. A diode rectifier bridge is therefor not suitable for the DTM test setup.

Throughout the sequence, a data acquiring system (DAQ system) together with sensors obtain voltage, current and rotor position measurement data. The obtained data from point 2) and 3), together with a post-processing system, derive information about the relationship between the stator currents and the linked magnetic flux. Figure 2.3 shows an example of a test sequence where measurements from the part within the yellow rectangle are used to derive the linked flux.

### 2.2.2 Current control

A prerequisite for the dynamic test method to work is a current controller that keeps the current to its reference value, even when the induced voltages in the stator windings change very fast. In addition, the controller must perform without knowledge of the magnetic model of the machine. To handle this problem, a direct current control (DCC) scheme - a design which keeps the current within hysteresis limits by picking a voltage vector which imposes a suitable current derivative - is used.

The DCC designs are known for being robust and to have fast transient current response. The hysteresis limits of the controllers may be implemented directly on the three phases, in the $\alpha\beta$ frame or in the $dq$ frame [19], [20], [21], [22]. Traditionally, the schemes have been designed for analog electronics since the reaction time in choosing voltage vector needs to be very fast, but the development of high speed AD converters and logic circuit technology has made high performance digital designs easier to implement [23], [24].

This section presents a scheme which suits the DTM test procedure well. It was created for a field programmable gate array (FPGA), which was used as the core of the experimental testing control system setup throughout this project. Hopefully the section gives the reader ideas of how a suitable DTM current control algorithm can look like, even if the FPGA technology is not available.

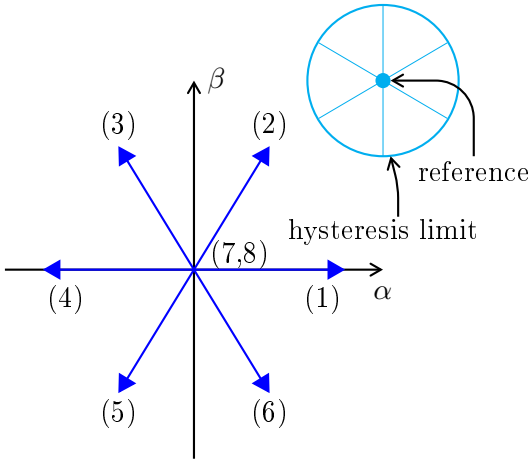


Figure 2.4: Converter voltage vectors together with the hysteresis limit, shown in blue, and the reference value, shown as a filled blue circle in the middle of the hysteresis limit. The limit is designed so the voltage vector which is chosen tracks the current towards the reference; for example, if the measured current is far right of the reference value, the algorithm applies vector (4)

### Hysteresis design

The DCC concept builds on the possibility to control the derivatives of the currents by choosing appropriate converter voltage vectors. The voltage equations for the PMSM in the $\alpha, \beta$ frame give expressions for the derivatives of the $\alpha, \beta$ currents

$$u_\alpha = R_s i_\alpha + L\frac{di_\alpha}{dt} - \omega\left(Li_\beta + \psi_m \sin\theta\right) \tag{2.7}$$

$$u_\beta = R_s i_\beta + L\frac{di_\beta}{dt} + \omega\left(Li_\alpha + \psi_m \cos\theta\right) \tag{2.8}$$

$$\rightarrow$$

$$\frac{di_\alpha}{dt} = \frac{u_\alpha + \omega\left(Li_\beta + \psi_m \sin\theta\right) - R_s i_\alpha}{L} \tag{2.9}$$

$$\frac{di_\beta}{dt} = \frac{u_\beta - \omega\left(Li_\alpha + \psi_m \cos\theta\right) - R_s i_\beta}{L} \tag{2.10}$$

The expressions above show that depending on which voltage vector that the control algorithm chooses to use, the currents can be controlled to track in a certain direction in the $\alpha, \beta$ frame. If the current deviates from the reference value, some of the voltage vectors move the current in the wanted direction. The DCC algorithm can therefore be designed to pick the best vector possible as soon as the current error is so big that the current tracks outside of the hysteresis limit.

Figure 2.4 shows the hysteresis limit that dictates when the control system reevaluates which voltage vector it applies. The limit is circular to make the error as uniformly distributed as possible. The control system picks vector depending on the angle of the error in regard to the $\alpha$ axis. Once the current tracks outside of the circle, the algorithm chooses a new vector to decrease the error. The controller keeps the same vector until the current tracks outside of the limit once again, whereupon the choice of vector is reevaluated.

*Utilizing the zero vector*

In contrast to a PWM modulated control, the DCC introduces a variable converter switching frequency. This can become problematic as high current derivatives lead to a high switching frequency. A way to improve the design in this aspect is to introduce a second hysteresis limit which decides when to chose the zero vector. The zero vector does not apply any voltage from the converter on the phase windings. Instead, the induced voltage from the induction in the stator windings creates a

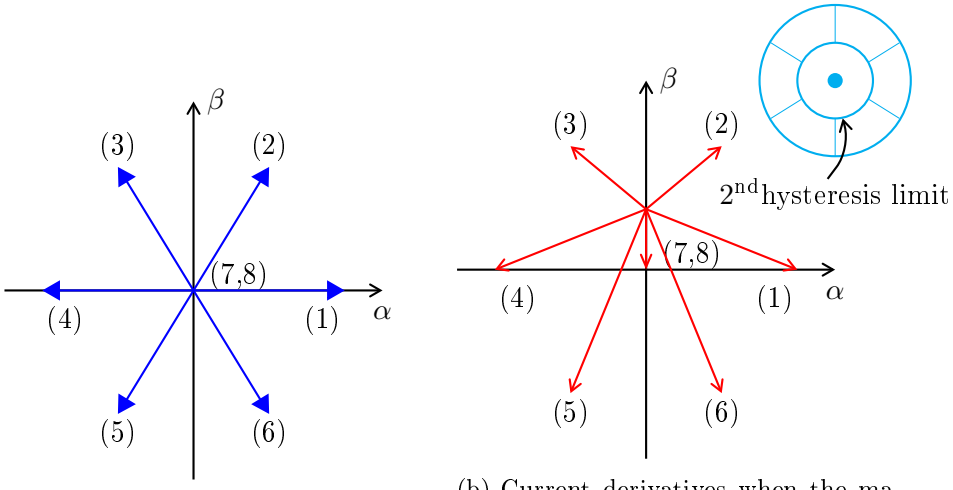


(a) Converter voltage vectors

(b) Current derivatives when the machine rotates. The zero vectors (7,8) change the current due to the induced voltage

Figure 2.5: Voltage vectors, current derivatives and hysteresis limits

change in the current. Since the induced voltage is smaller than the active vectors at low speed, the derivative of the current becomes smaller, and the switching frequency consequently decreases. When the speed increases, the zero vector – which the controller picks to track the current towards origo in the $\alpha\beta$ plane – is still smaller than the active vectors that drive the current in the same direction.

Figure 2.5b shows a double limit hysteresis design. If the error is zero from the beginning but increases, nothing happens until the current passes the outer limit whereat the algorithm chooses a suitable active vector (1..6). The error then starts to decrease until the current crosses the inner hysteresis ($2^{\text{nd}}$) limit. Eventually the error starts to grow again until the inner limit is passed once more; now the control system applies a zero voltage vector (7,8) until current passes the outer limit, and the process starts over.

Figure 2.6 shows a flow-chart of the controller. The reference value is given in $dq$ coordinates and is then transformed to the $\alpha, \beta$ frame (not

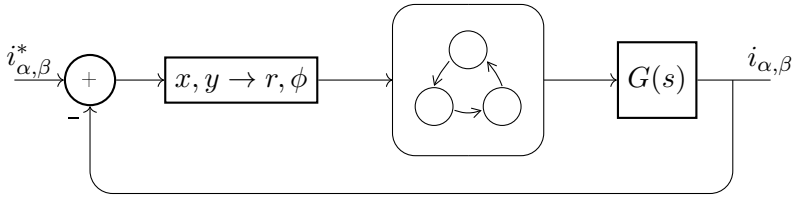


Figure 2.6: Flowchart of the direct current control in $\alpha\beta$ coordinates. The box after the subtraction represents a transformation from Cartesian to polar coordinates

shown in the figure). This becomes the reference input to the algorithm. The error in $\alpha, \beta$ Cartesian coordinates is transformed to polar coordinates, and the resulting angle and magnitude are fed into the state-machine which decides which vector that should be chosen for the next time instant.

### EMF compensation

Since the induced voltage drags the current towards origo in the $\alpha\beta$ frame, the inner hysteresis limit gives rise to a current error. Furthermore, an increased speed tend to worsen this error since the active vectors lose the capability to drive the current away from origo. Figure 2.5b – which shows the resulting current derivatives for each converter voltage vector – explains the phenomenon. In the figure, the machine rotates, and the resulting emf drives the current towards origo when the control system chooses a zero vector (7,8). If the current hits the lower part of the outer hysteresis limit, the algorithm picks vector 2 or 3 to drive the current away from origo. Since the zero vector current derivative affects the direction of the active vector current derivatives, vector 2 and 3 drive the current to the side of the hysteresis limits rather than the top. Therefore, the current get stuck in the lower part of the two hysteresis circles. This introduces an error in regard to the reference. In $\alpha\beta$, the error is varying with the rotor position, but the magnitude of the error is approximately proportional to speed. Therefore, the average error in $dq$ coordinates is independent of rotor position but affected by

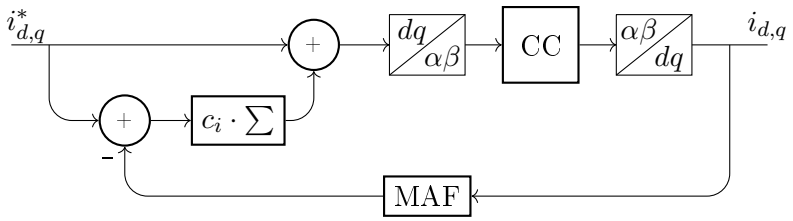


Figure 2.7: Complete algorithm with moving hysteresis limits

the speed.

Moving hysteresis limits provide a solution to this problem. The reference value, which is in the middle of the two hysteresis circles, adjusts itself to make sure that the average value of the measured current does not deviate from the reference. A moving average filter together with an integrator make this possible. Figure 2.7 shows a flow-chart of the control algorithm when the moving hysteresis bands are introduced. The integration of the error, multiplied by a gain, adjusts the reference value to minimize the offset. To derive the current error, the moving average filter first reduces the current ripple of the measured current, whereupon it is subtracted from the reference. The time constant of the filter and the accumulation gain should be scaled so the compensation is fast enough to react on the mechanical dynamics, but not fast enough to become sensitive to electrical dynamics.

*Choice of gains*

For the emf compensation algorithm to work well, the filter and accumulation gain need to be scaled properly. Too high gains make the system unstable, while too small gains lead to bad performance. With a sufficiently high sampling frequency, the converter switching frequency dictates the limit for the bandwidth of the filter and the integrator. The moving average filter is mathematically expressed as

$$h(n) = \frac{1}{N} \sum_{k=0}^{N-1} \delta[n-k] \tag{2.11}$$

where N is equal to the number of elements. Written in frequency domain, the transfer function becomes

$$H(\omega) = \frac{1}{N} \sum e^{-j\omega n} \tag{2.12}$$

which with Euler identity may be rewritten as

$$H(\omega) = \frac{1}{N} \left| \frac{sin\frac{wn}{2}}{sin\frac{w}{2}} \right| \tag{2.13}$$

where $\omega$ is equal to the cut-off frequency divided by the sampling frequency times two pi. The cut-off frequency is when $H(\omega) = \frac{1}{\sqrt{2}}$, and the $N$ which satisfies (2.13) is the number of elements used in the filter. Simulations show that

$$\omega_b = \frac{\omega_{sw}}{10} \tag{2.14}$$

where $\omega_{sw}$ is the converter switching frequency is a suitable cut-off frequency for the filter. The integral gain is then chosen as 10 times smaller than $\frac{1}{N}$

$$c_i = \frac{1}{10 \cdot N} \tag{2.15}$$

### 2.2.3 Deriving the linked flux

Once the measurement data is acquired, the linked magnetic flux is derived from the measured voltages, the measured currents and the

rotor position. A rewrite of (2.5) and (2.6) yields expressions for the flux

$$\psi_q^{\left(i_d^\psi, i_q^\psi\right)} = \frac{u_d - R_s i_d^s}{\omega} \tag{2.16}$$

$$\psi_d^{\left(i_d^\psi, i_q^\psi\right)} = \frac{-u_q - R_s i_q^s}{\omega} \tag{2.17}$$

The equivalent circuit of the machine (Fig. 2.2) shows that the iron losses influence the linked flux differently if the machine works as a generator or as a motor. If the currents are held constant, the induced voltages change sign depending on the working regime. This means that the currents that flow through the equivalent eddy current resistances change sign.

Even if the sign of the induced voltages vary, the magnitudes of them – and the size of the eddy current resistance – are approximately the same when the magnitude of the electric frequencies are equal, regardless if the machine works as a generator or as a motor. As a consequence, the magnitude of the eddy current loss currents are also approximately equal under the same conditions, and hence follows

$$i_d^s \approx \frac{i_{d,motor}^\psi + i_{d,generator}^\psi}{2} \tag{2.18}$$

$$i_q^s \approx \frac{i_{q,motor}^\psi + i_{q,generator}^\psi}{2} \tag{2.19}$$

for each electrical frequency. Supposing that the flux which is generated from $i_{motor}^\psi$ and $i_{generator}^\psi$ has a linear relationship to the currents, (2.18) and (2.19) can be directly translated to expressions for the flux

$$\psi_d^{\left(i_d^s, i_q^s\right)} \approx \frac{\psi_{d,motor}^{\left(i_d^\psi, i_q^\psi\right)} + \psi_{d,generator}^{\left(i_d^\psi, i_q^\psi\right)}}{2} \tag{2.20}$$

$$\psi_q^{\left(i_d^s, i_q^s\right)} \approx \frac{\psi_{q,motor}^{\left(i_d^\psi, i_q^\psi\right)} + \psi_{q,generator}^{\left(i_d^\psi, i_q^\psi\right)}}{2} \tag{2.21}$$

Combining (2.16) and (2.17) together with (2.20) and (2.21), expressions for the flux using measurements from both when the machine is accelerating and when it is braking are reached

$$\psi_q^{\left(i_d^s, i_q^s\right)} \approx \frac{\frac{u_d^\omega - R_s i_d^s}{\omega} + \frac{u_d^{-\omega} - R_s i_d^s}{-\omega}}{2} = \frac{u_d^\omega - u_d^{-\omega}}{2\omega} \tag{2.22}$$

$$\psi_d^{\left(i_d^s, i_q^s\right)} \approx \frac{\frac{-u_q^\omega - R_s i_q^s}{\omega} + \frac{-u_q^{-\omega} - R_s i_q^s}{-\omega}}{2} = \frac{-u_q^\omega + u_q^{-\omega}}{2\omega} \tag{2.23}$$

Deriving the flux in this way has some noteworthy implications:

1. The equations yield the average value of the flux when the machine works as a generator and a motor, for the same stator winding currents.

2. Information about the stator winding resistive voltage drop is not needed for calculations of the linked flux. This is true only if the temperature rise in the windings is insignificant during one test cycle.

3. The linked flux is constant over the whole frequency range. This makes it possible to use a lot of measurements during one speed sequence, which can be averaged for a better result.

Figure 2.8 shows an example of the $d$ flux linkage results for a typical test sequence. The red line is the first term of the numerator on the

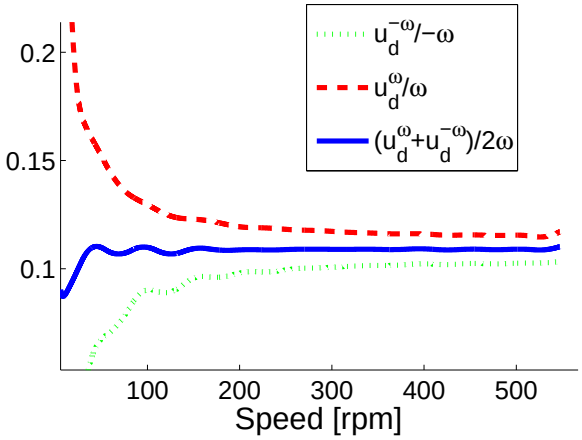


Figure 2.8: Flux derivation using the dynamic test method. The red line is the first term in the denominator of the right hand side in (2.22), the blue line is second, and the green is the result from the total expression

right hand side of (2.22), which represents the accelerating part of the sequence (where the machine works as motor). The blue line is the second term, which represent the braking part. The green line is the mean value of the two which is the total results of the right hand side of (2.22). As the results become unstable when approaching zero speed, it is recommended that measurements when the speed is low are not used for the derivation of the flux.

## 2.3 Torque derivation

### 2.3.1 Air-gap torque

In addition to linked magnetic flux maps, the dynamic test method provides the torque characteristics of the test object. The flux for a specific current combination together with the currents yield the air-

gap torque in between the rotor and the stator. The equation for the air-gap torgue can be deduced from the electric power

$$P_e = u_a i_a + u_b i_b + u_b i_b \tag{2.24}$$

Transforming the voltage and current with the power-invariant transform ($K = \sqrt{\frac{2}{3}}$), (2.24) together with (2.1) and (2.2) yield

$$P_e = u_d i_d^s + u_q i_q^s \tag{2.25}$$

Removing the copper losses in the stator windings, which do not contribute to any torque, (2.25) with (2.5) and (2.6) become

$$P_e = \omega(-\psi_q^{\left(i_d^\psi, i_q^\psi\right)} i_d^s + \psi_d^{\left(i_d^\psi, i_q^\psi\right)} i_q^s) \tag{2.26}$$

Power can also be expressed as force times speed, or in this case, the torque times the frequency

$$P_e = T_{ag}\omega \tag{2.27}$$

Combining (2.26) with (2.27), a final expression for the electromagnetic torque in the air-gap is reached

$$T_{ag} = \psi_d^{\left(i_d^\psi, i_q^\psi\right)} i_q^s - \psi_q^{\left(i_d^\psi, i_q^\psi\right)} i_d^s \tag{2.28}$$

Using the derived flux from the DTM, the mean torque for the motor and the generator operation for every current combination in the $dq$ frame is derived by

$$T_{ag}^{m} = \psi_{d}^{\left(i_{d}^{s}, i_{q}^{s}\right)} i_{q}^{s} - \psi_{q}^{\left(i_{d}^{s}, i_{q}^{s}\right)} i_{d}^{s} \tag{2.29}$$

### 2.3.2 Rotor shaft torque

Newton's second law gives a relationship between the acceleration of an object with a specific mass when it is exposed to a force

$$F = ma \tag{2.30}$$

If an additional force in the opposite direction of the first affects the system, the equation can be extended to

$$F = ma + F_{ext} \tag{2.31}$$

where $F_{ext}$ is the additional force that is imposed on the object. Considering a cylinder – as the rotor in a PMSM – (2.31) can be translated to

$$T_{rs} = J\frac{d\omega_m}{dt} + T_{ext} \tag{2.32}$$

where $T_{rs}$ is the rotor shaft torque, which is the resulting tangential radial force that acts on the rotor shaft times the radius of the rotor (the force that makes the cylinder rotate around it's central axis); $J$ is the rotor shaft moment of inertia; $\frac{d_{\omega_m}}{dt}$ represents the acceleration of the mechanical frequency of the rotor; and $T_{ext}$ is an external torque on the rotor. In a PMSM, the rotor shaft torque can be divided up into two main components: the air-gap torque $T_{ag}$, and the mechanical loss torque $T_{loss}$.

$$T_{ag} - T_{loss}^{mec} = J\frac{d\omega_m}{dt} + T_{ext} \tag{2.33}$$

The external torque is a load when the machine works as a motor, and a driving torque when the machine works as a generator. In the DTM, neither a drive nor a load is connected to the rotor shaft, and consequently $T_{ext}$ is zero. The loss torque brakes the machine in the motor regime, which means that the air-gap torque and the loss torque have different signs. In the generator regime on the other hand, the loss torque has the same sign as the air-gap torque. This means that if the magnitude of the loss torque is considered independent of the rotational direction, it is canceled if the calculation uses measurements from both the motor and the generator operation, as long as the frequency and the air-gap torque, which means $dq$ currents, are the same. The air-gap torque for one $dq$ current combination becomes

$$T_{ag}^{m} = J\frac{\frac{d\omega_{m,motor}}{dt} + \frac{d\omega_{m,generator}}{dt}}{2} \tag{2.34}$$

Figure 2.9 shows an example of how the mean torque over a speed sequence is derived. When the machine works as a generator (blue line) the torque is higher since the loss torque has the same sign as the electromagnetic torque. When the speed increases, the torque increases as well as the iron losses and the mechanical losses are speed dependent. On the other hand, when the machine works as a motor (red line), the loss torque works against the acceleration, and the resulting torque becomes lower. The green line is the mean value of the two cases, and is independent of speed. When the speed approaches zero, the results oscillates, and it is recommended to not include low speed measurements in the torque derivation.

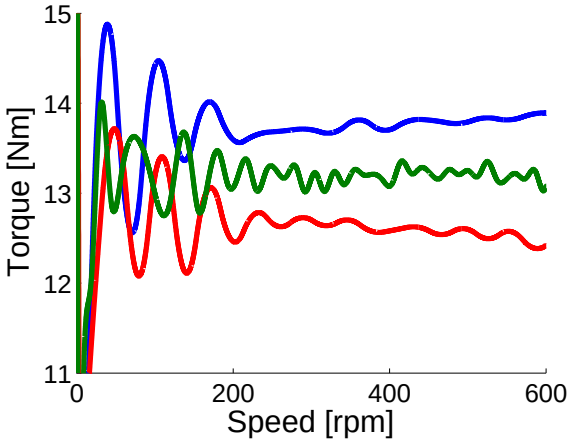


Figure 2.9: Mechanical torque derivation using the dynamic test method. The blue line is when the machine works as generator, the red line when it works as a motor, and the green line is a mean value between the two

### Derivation of moment of inertia

To derive the shaft torque, (2.34) needs information about the test object's rotor shaft moment of inertia. Since this information is not always available, it is necessary to find a way to derive it. This is not trivial, specially if the test object is an unknown machine where the rotor geometry is not known. The method which has been used in this project derives the rotor moment of inertia using flywheels which are designed to mount on the rotor shaft. Figure 2.10a shows an example of typical flywheels that may be used for the moment of intertia derivation. The first step of this method is to find the moment of inertia of the flywheels themselves.

A flywheel's moment of inertia can be derived with a trifiliar pendulum [25]. Figure 2.10b shows a typical pendulum that works well for this application. First and foremost, the moment of the inertia of the pendulum itself must be derived. The weight of the triangular base plate $m_p$, the length of a wire $l$, the length from the middle of the base plate

(a) Flywheels

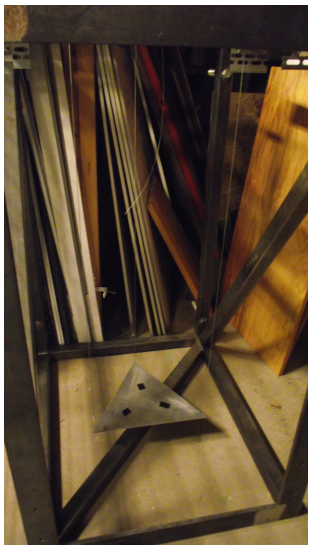

(b) Trifiliar pendulum

Figure 2.10: Typical flywheels and a pendulum which can be used to derive the rotor moment of inertia

to a wire $r$, the gravity $g$, and the period time when the pendulum is set in motion $\tau$ determine the pendulums moment of inertia according to

$$J_p = m_p \frac{r^2 \tau^2 g}{4\pi l} \tag{2.35}$$

Once $J_p$ is known, the masses of the flywheels establish their moment of inertia as

$$J_f = (m_p + m_f) \frac{r^2 \tau^2 g}{4\pi l} - J_p \tag{2.36}$$

When the moment of inertia of the flywheels are known, an extrapolation of a series of accelerations with the different flywheels mounted on

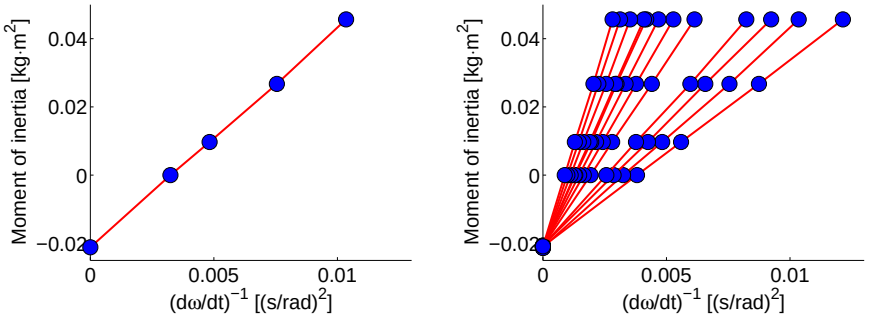


(a) Moment of inertia extrapolation with on torque

(b) Moment of inertia extrapolation with several torques

Figure 2.11: Extrapolation of the rotor moment of inertia using three flywheels. One red line represents one specific torque, while the blue dots along the red lines are the different moments of inertia

the rotor shaft ascertains the PMSM's rotor moment of inertia. Figure 2.11a shows an example of the procedure. The red line is an interpolation of $J$ as a function of the inverse of $\frac{d\omega}{dt}$ when the same torque accelerates the machine with four different moment of inertia on the rotor shaft (three cases with different flywheels mounted and one case without flywheel). The line also extends to extrapolate the rotor moment of inertia, which is when $(\mathrm{d}\omega/\mathrm{dt})^{-1}$ is zero. Figure 2.11b shows the rotor moment of inertia derivation when several different torques are used. All extrapolations converge towards the same point; this is the moment of inertia of the rotor.

When the moment of inertia estimations for a satisfying amount of different torques on the rotor shaft are available, the mean value of the results is calculated according to

$$\overline{y} = \frac{1}{n} \sum_{i=1}^{n} y(i) \tag{2.37}$$

To get a notion of how much the different inertia estimation differ, the standard deviation of the result can be calculated according to

$$\sigma = \sqrt{\frac{1}{n-1}\sum_{i=1}^{n}(y(i)-\overline{y})^2} \tag{2.38}$$

### 2.3.3 Conclusions

As the previous sections show, both the flux and current and the moment of inertia and acceleration can derive the mean air-gap torque ($T_{ag}^{m}$). As a consequence, the moment of inertia can be derived directly from the DTM measurements since

$$J\frac{\frac{d\omega_{m,motor}}{dt}+\frac{d\omega_{m,generator}}{dt}}{2} = \psi_d^m i_q - \psi_q^m i_d \tag{2.39}$$

$$J = \frac{2(\psi_d^{(i_d^s,i_q^s)} i_q - \psi_q^{(i_d^s,i_q^s)} i_d)}{\frac{d\omega_{m,motor}}{dt}+\frac{d\omega_{m,generator}}{dt}} \tag{2.40}$$

The moment of inertia derivation above makes it possible to obtain the rotor shaft torque both for when the machine works as a motor and as a generator without the need of a pendulum and flywheels or knowledge about the rotor geometry. Consequently, the loss torque can be quantified without a pendulum and flywheels or knowledge about the rotor geometry.

With the straight forward way to derive the moment of inertia which (2.40) introduces, it may seam unnecessary to include the additional method (presented in the previous section). The additional method is included due to uncertainty regarding accuracy. Chapter 4 presents a consistency analysis to control whether the (2.40) can derive $J$ accurately or not (section 4.2.3).

## 2.4 Efficiency tests

### 2.4.1 Test procedure

The DTM needs a second iteration of experimental tests to derive the efficiency of the test object. There are two main reasons why the results from the first test cycles – described in subsection 2.2.1 – can not be reused

1. The first iteration of cycles does not test the machine at very high speeds. Since the speed's limit is set manually to a value which assures that the induced voltage does not reach the voltage limit, higher speeds are left out.

2. The current controller which is used in the magnetic model identification works with a variable frequency (section 2.2.2 describes the current controller), which makes it problematic to measure the quasi-instantaneous voltage accurately. This is not a problem when the magnetic flux linkage is derived since many measurements can be average to derive an accurate result, but the efficiency derivation demands accurate voltage measurements throughout the test sequence.

#### Finding the maximum speed

The first challenge for the design of the new test sequence is thus to find the maximum possible speed for each testing point. The maximum speed varies depending on the stator current. One approach to find the speed limit is to calculate an estimation of the maximum frequency from (2.5) and (2.6) (this demands that the stator resistance is estimated beforehand). The DTM magnetic model derivation provides the linked magnetic flux, and the DC link voltage of the drive defines the maximum voltage. The modulus of the $dq$ voltage phasor is expressed as

$$|u_{dq}| = \sqrt{u_d^2 + u_q^2} \tag{2.41}$$

substitution of $u_d$ and $u_q$ with the expressions on the right hand sides of (2.5) and (2.6) yield

$$|u_{dq}| = \sqrt{(R_s i_d - \omega\psi_q)^2 + (R_s i_q + \omega\psi_d)^2} \tag{2.42}$$

Assuming $|u_{dq}|$ is the maximum voltage ($|u_m|$), the frequency is the only unknown variable in (2.42). A rewrite of (2.42) yields a second order equation of $\omega$ with only one positive solution

$$\omega_{\max}(i_d^s, i_q^s) = \frac{R_s}{|\psi_{dq}|^2}\left(\sqrt{|\psi_{dq}|^2(|u_m|^2 - |i_{dq}|^2) + (i_q\psi_d - i_d\psi_q)^2} - (i_q\psi_d - i_d\psi_q)\right) \tag{2.43}$$

The expression above derives the maximum speed for the fundamental frequency of the induced voltage, but since the induced voltage always carries harmonics, the calculations tend to overestimate the speed limit. A scaling factor below one provides a safety margin, but since the harmonic content of the induced voltage differs depending on current combination, a suitable value of the scaling factor can be hard to find.

A second method to derive the maximum speed controls if the reference voltage value from the controller output reaches the maximum allowed value. This is a straight forward on-line method, and if the algorithm sets the limit as a function of the DC link voltage, it takes fluctuations in that voltage level into account. The reference depends heavily on the gains of the controller, and high P gains can lead to big ripples. As a consequence, the algorithm tends to limit the speed at an unnecessary low value. This can be taken into account for with a low-pass filter, but the filter must not be slow to underestimate the induced voltage. If the bandwidth of the filter is known, the delay can be taken into account for by a set limit between the maximum allowed voltage and the filtered

reference value. The method can be further enhanced if the dead time and the rise and fall times of the IGBTs are taken into account.

Another approach is to try to find the speed limit experimentally – this is the method the tests used throughout this project. Experimental tests provide information about the maximum speed for a current combination when the controller no longer can keep the currents to their reference. This is a dangerous way of investigating the maximum speed since the field weakening current must be maintained at high speeds. If the current controller fails to maintain $i_d$, the induced voltage may rise above the drive's maximum available voltage, which can have severe consequences such as demolition of the drive's DC link capacitor bank.

A specially designed prioritization algorithm in the current controller solves this problem: An observer constantly checks how much the average value of the modulus of the $dq$ current deviates from the reference. If the current deviates too much, the controller lowers the modulus and changes the sign of the $q$ current – the smaller current makes sure that the voltage limit is not breached. The new current combination generates a negative torque which brakes the machine until the rotor stands still whereupon the controller sets the reference to zero. The point where the current starts to deviate gives the information about the maximum speed. Since this point is on the very limit of the availible voltage, the limit should be reduced with a constant value to make sure that the control of the field weakening current is not lost.

A current controller which is fast and robust is a necessity for this algorithm. Since the controller which is used in the magnetic model identification test procedure fulfills these criteria, it can advantageously be reused for these tests.

### Switching current controller

Despite the advantages of the DCC scheme, the variable switching frequency which the method gives rise to makes it to hard to measure

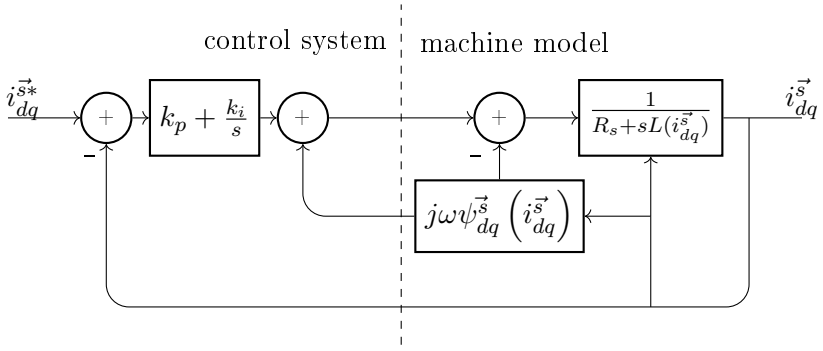


Figure 2.12: Flowchart of the field oriented vector controller

the converter voltages over small time windows accurately. Since the efficiency measurements need good quasi-instantaneous voltage measurements, a well performing DTM needs an additional current control method for the efficiency testing.

The field oriented PI current controller in the rotating coordinate system is a well established strategy for controlling currents in electrical machines [26]. The control system controls the drive's converter with pulse width modulated signals which means that the switching frequency can be constant. Figure 2.12 shows a flowchart of the controller applied on a non-linear PMSM. The machine is modeled in polar coordinates instead of the Cartesian so one flowchart is enough to describe the system. The variable $\vec{i_s}$ is defined as

$$i_{dq}^{\vec{s}} = |i_{dq}^{\vec{s}}|e^{j\alpha} \begin{cases} \alpha = \tan^{-1}\frac{i_q}{i_d} \\ |i_{dq}^{\vec{s}}| = \sqrt{i_d^2 + i_q^2} \end{cases}$$

The definition leads to the voltage equation

$$v_{dq}^{\vec{s}} = R_s i_{dq}^{\vec{s}} + L(i_{dq}^{\vec{s}})\frac{di_{dq}^{\vec{s}}}{dt} + j\omega\psi_{dq}^{\vec{s}}(i_{dq}^{\vec{\psi}}) \tag{2.44}$$

where $\vec{\psi^s_{dq}}$ is the total linked flux vector which includes both the permanent magnet flux and the flux due to the stator currents. The equation above describes the stator current's relationship with the drive's voltage, which is controlled by the control system. Note that (2.44) expresses the derivative of the flux $\frac{d\psi_s}{dt}$ as an inductance times the derivative of the current. This paraphrasing makes it possible to express the machine as a RL load, which is valuable when deciding the gains of the controller. A laplace transformation of the equation above yields the expression for the load in the frequency domain

$$\frac{I^s_{dq}(s)}{U^s_{dq}(s) - j\omega\Psi^s_{dq}(s)} = \frac{1}{R_s + Ls} \tag{2.45}$$

Due to the non-linearity of the machine's flux linkage, the inductance – and also to a certain extent the flux linkage of the permanent magnets – is dependent on the stator current. Therefor, no load disturbance or pure feed-forward exist in this model (in most cases, these type of controls see the induced voltage due to the permanent magnet flux as a load disturbance which can be feed-forwarded without knowledge about the stator current). On the other hand, since the magnetic model derivation provides flux maps as functions of the stator currents, information about the flux linkage and inductance can be obtained by look-up tables. When the scheme in Figure 2.12 adds the induced voltage to the output signal of the control system, the PI controller only acts on the voltage over the RL load; the removal of the induced voltage from the system means that it is no longer affected by the mechanical dynamics. Note that the look-up table approach – in contrast to the more conventional use of constant values for the inductance and the linked permanent magnet flux – takes the magnetic non-linearity due to saturation in the core of the machine into account.

*Choosing PI gains*

As mentioned above, the PI controller only acts on the system as a RL load. With this in mind, the proportional and integral gain can be determined so that only one pole exists in the whole closed loop system.

The internal model control (IMC) method provides the necessary steps to obtain the gains with the possibility to chose the bandwidth of the system[27].

As the control scheme removes the induced voltage from the closed loop system, the open loop transfer function of the machine model becomes

$$G(s) = \frac{1}{R_s + sL} \tag{2.46}$$

On the control system side, the open loop transfer function becomes

$$F(s) = k_p + \frac{k_i}{s} \tag{2.47}$$

The complete closed loop transfer function of the system is formulated as

$$T(s) = \frac{G(s)F(s)}{1 + G(s)F(s)} \tag{2.48}$$

To achieve a one pole system, the transfer function is also described as a first order low-pass filter

$$T(s) = \frac{\frac{\alpha}{s}}{1 + \frac{\alpha}{s}} \tag{2.49}$$

where $\alpha$ is the bandwidth of the filter. The combination of (2.48) and (2.51) yield

$$\frac{\alpha}{s} = G(s)F(s) \tag{2.50}$$

which means that

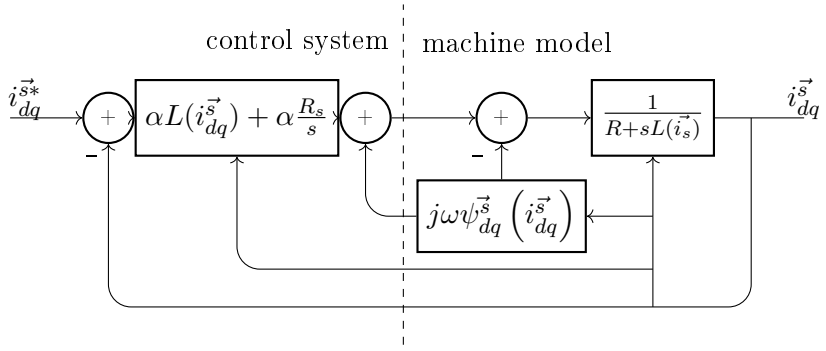


Figure 2.13: Updated flowchart of the field oriented vector controller

$$F(s) = \frac{\alpha}{s}G(s)^{-1} \tag{2.51}$$

which, with a combination of (2.46) and (2.47), gives

$$k_p + \frac{k_i}{s} = \alpha\left(L + \frac{R_s}{s}\right) \rightarrow \begin{cases} k_p = \alpha L \\ k_i = \alpha R_s \end{cases}$$

Figure 2.13 shows an updated version of the closed loop system. Notice that the proportional gain of the PI controller is dependent on the stator current which means that the control system updates $k_p$ every sampling period. The bandwidth $\alpha$ decides the dynamics of the system and is limited by the switching frequency of the drive's converter and the sampling frequency. In addition to what is included in the flowchart, the controller also includes limits for the output from the PI controller and an anti windup algorithm which makes sure that the integral part stops accumulating error if the output hits the limit. The implementation of these attributes together with guidelines for the choice of bandwidth is presented in [27].

It should be emphasized that this section only presents a suggestion for a current control algorithm for the DTM efficiency test sequence. Since properties of the current controller affect the efficiency of the machine in

itself, it is optimal if the test sequence uses the same current controller which is used in the test objects intended application [28], [29], [30].

#### Final test algorithm

The subsections above give solutions for the problems that the efficiency tests introduce. With the solutions in mind, the final test sequence for the efficiency evaluation becomes

1. The maximum speed is evaluated by the preferred method (by experimental means in this work).

2. The control system switches current control method from the DCC to FOC. The voltage drive accelerates the machine to the maximum negative speed possible with the evaluated current combination, but with the $q$ current negated.

3. The control system switches sign on the $q$ current. The drive brakes the machine to zero speed, and accelerates it up to the maximum positive speed.

4. The drive brakes the machine to zero speed. Observe that the $d$ current (field-weakening current) must be maintained throughout the braking to make sure that the induced voltage do not exceed the DC voltage.

### 2.4.2 Theory of efficiency derivation

The efficiency of a PMSM is defined as the the output power divided by the input power. When the machine works as a motor, the expression for the efficiency is

$$\eta = \frac{P_m}{P_e} \tag{2.52}$$

where $P_m$ is the mechanical power on the rotor shaft and $P_e$ is the electrical output power from the drive system. When the efficiency for the generator is calculated, $P_m$ and $P_e$ switches place. The electrical power is given by (2.24), and the mechanical power is the rotor shaft torque times the mechanical frequency

$$P_m = T_{rs}\omega_m \tag{2.53}$$

where the acceleration and the rotor shaft moment of inertia give the shaft torque according to (2.32). Knowing that the mechanical angular frequency is the derivative of the rotor position divided by number of pole pairs in the machine, (2.27), (2.53), (2.32) and (2.54) yield an expression for the efficiency

$$\eta = J\frac{d\omega_m}{dt}\omega_m\frac{1}{u_a i_a + u_b i_b + u_c i_c} \tag{2.54}$$

where $p$ is the number of pole pairs in the machine.

### 2.4.3 Practical derivation of the efficiency from the measurement

The efficiency of a variable frequency drive machine is often presented as a function of torque and speed. Since many $dq$ currents achieve the same torque and speed combination in a PMSM, the choice of torque control algorithm influences the efficiency when the machine works in its application (this is especially true for salient pole PMSMs where the reluctance properties of the rotor contribute to the torque, and a $i_d^s = 0$ control strategy is highly inadvisable). Figure 2.14 shows the speed and torque characteristics for a typical salient pole PMSM. Numerous current combinations yield the same torque and have a maximum speed which needs to be taken into account for. Since the different current combinations yield different efficiencies, the first step to derive the DTM machine efficiency characteristics is to decide which currents that should be used.

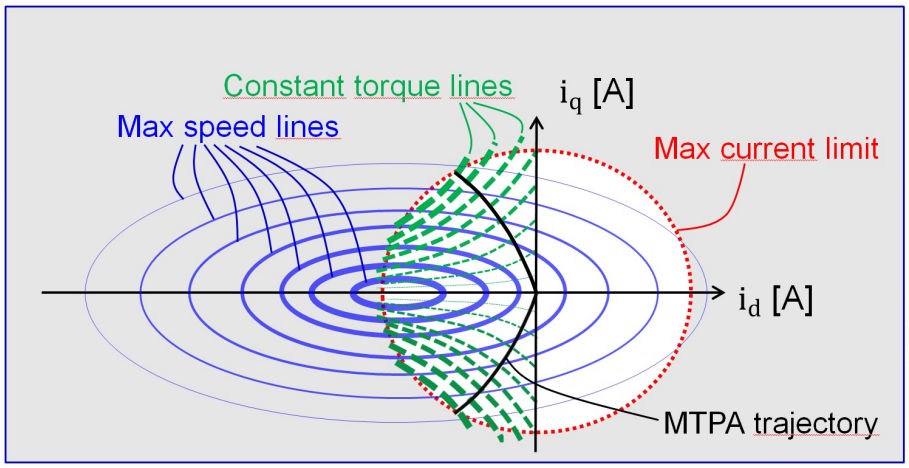


Figure 2.14: Constant torque lines and speed limit lines. Many current combinations yield the same torque which means that the efficiency is dependent on the torque control algorithm

Figure 2.14 also shows the Max Torque Per Ampere (MTPA) trajectory, which is a well established strategy for choosing current combination. The strategy uses the minimal current which achieves the desired speed and torque [31]. The method calculates the proper *dq* current references based on the torque equation of the PMSM, which means that the magnetic model and the resistance of the machine must be known. In recent schemes, online algorithms provide accurate estimation of the machine parameters for a better performing control [32], [33].

Another category of control schemes focuses on minimizing the losses. The methods use analytical expressions for the speed-dependent losses to derive the optimal point to minimize the loss (or maximize the efficiency) for each desired torque and speed combination [34], [35], [36]. The iron losses are hard to estimate analytically due to their highly nonlinear behavior, and the accuracy of the methods can therefore be questioned.

This work uses a method which derives the current combinations which provides the maximum efficiency for each torque without analytical

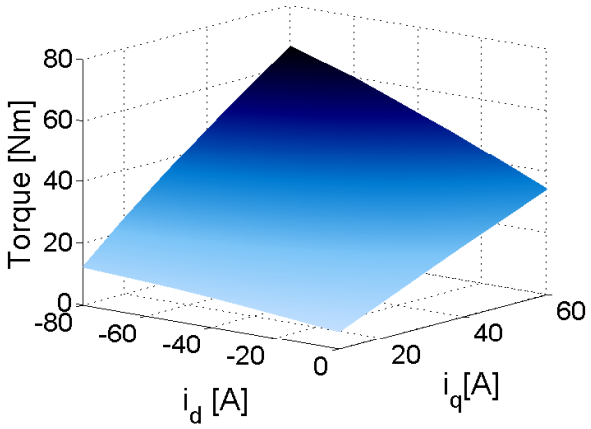


Figure 2.15: High resolution torque matrix

expressions. Here, the torques in the efficiency maps are the mean values of the motor and generator torque for each current combination (which approximates the air-gap torque). The reason for using the mean torque instead of the shaft torque is because the acceleration throughout the test sequence tend to oscillate, and a good torque estimation for each speed is therefor hard to obtain. Theoretically, it should be possible to use a third order polynomial to approximate the evolution of the torque over the speed range accurately, but experimental results show that this is not always the case.

The first step to derive the efficiency map is to find the torque characteristics of the machine. Section 2.3.2 presents the procedure to obtain the torque from the magnetic model derivation measurements. The efficiency algorithm performs an interpolation of the torque results to create a fine resolution matrix as function of the $dq$ currents. Figure 2.15 shows an example of the high resolution matrix which the algorithm creates. As mentioned in section 2.3.2, the results are independent of the rotor speed.

In the second step, the algorithm calculates the efficiency as a function of speed for each measured $dq$ current combination from (2.54). Due to

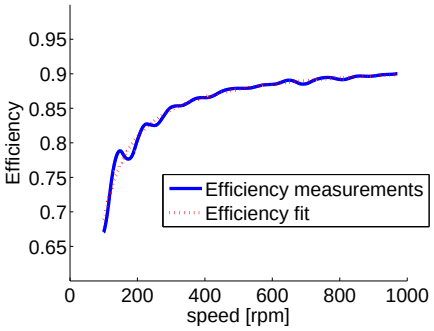


(a) Efficiency as a function of speed for one specific current combination

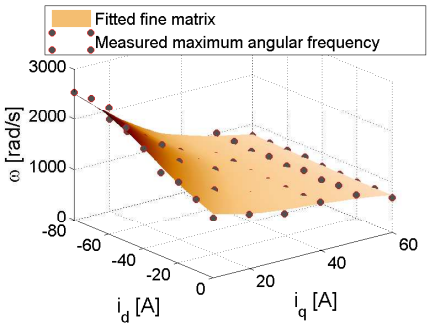


(b) Maximum speeds for each current combination

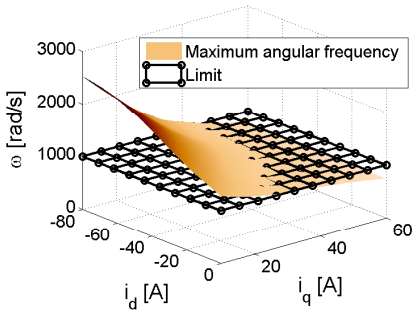


(c) the maximum speeds at 1000 rad/s. Only the current combinations which have a maximum speed over the limit may be used

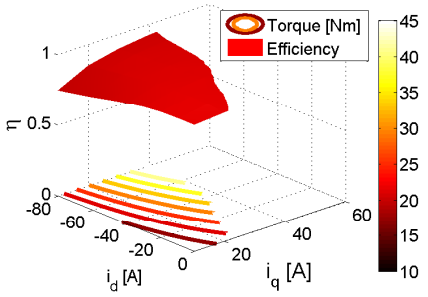


(d) The torque and efficiency of the available current combinations

Figure 2.16: Graphical explanations of steps to reach the efficiency as a function of torque

the oscillations of the obtained measurements, they can not be directly used. However, in this case – in contrast to the case of the shaft torque – a two term exponential fit of the results gives a decent approximation of the efficiency for each speed. Figure 2.16a shows how a fit compared with the obtained measurements can look like. The measurements start at 100 rpm which in this case is the lower speed limit of the efficiency derivation.

In the next step the max speed for each current combination is fitted into a polynomial. The function gives an estimation if a current combination somewhere within the maximum currents can be maintained for a certain speed or not. Figure 2.16b shows an example of the function for the measured maximum speeds and the polynomial fit. Even if the results from the pylonomial fit diverges a bit from the measured points, the approximation is still fairly accurate. Ideally more current combinations should be measured for a better result. When the max speed for each current combination is known, it is straight forward for the algorithm to derive the available current combinations for the speed which it evaluates. Figure 2.16c shows an example of the process. The machine only operates within the area which is above the speed limit.

With the results from Figure 2.16a and Figure 2.16c, the algorithm derives an efficiency map as a function of the available mean air-gap torque. Figure 2.16d shows the resulting efficiency together with torque lines. An infinite amount of current combinations create the available torque, but an optimization algorithm finds the current combinations which yield the available torques with the highest efficiencies. The algorithm iterates through the speeds that the user desires to evaluate, and creates an efficiency map as a function of torque and speed. The efficiency measurement section of chapter 4 presents a graphical representation of the end result of the procedure.

### 2.4.4 Power Factor

The power factor (PF) is defined as the cosinus of the angle between the fundamental components of the terminal voltage and current, and is thus a measurement on how much of the apparent power from the converter that becomes heat and work in the machine. The most forward way to derive the power factor is to do a Fast Fourier Transform (FFT) on each period of the measured signals and derive the phase angle in between them. This method can be problematic as the induced voltage can contain a lot of harmonics – especially in high field-weakening operating where the permanent magnet flux interacts with the flux created by the $d$-current – which leads to high frequency components in the

voltage, and also to a certain extent in the current. This in turn makes it hard to distinguish the transition between the different periods in the signals.

A way to get around this problem is to first integrate the phase current and voltages before deriving the angle between the fundamental components of the signals. By doing so, the high frequency components of the signals get attenuated, since

$$\int \sin \omega t \; dt = -\frac{1}{\omega} \cos \omega t + C \tag{2.55}$$

Figure 2.17 shows a comparison between untreated and integrated voltage and current signals when a machine works in deep field-weakening. The fundamental component of the voltage is barely distinguishable before the integration, but afterwards the fundamental is clearly dominating. This makes it easier for the post-processing algorithm to distinguish when a new period starts as the signal does not flicker around zero.

One aspect of this process which needs to be taken into account for is the

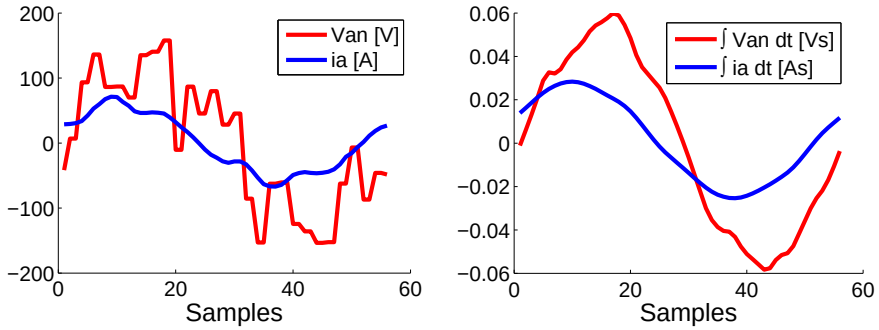


(a) Voltage and current (b) Integral of voltage and current

Figure 2.17: One fundamental period of voltage and current measurements in high field weakening

implications of a DC offset in the measurements. An offset leads to continuously growing ramps in the integrated signals. The imposed growing offset makes it hard to sort out the periods for the post-processing algorithm, and the DC component should therefor be filtered away before the integration is made. Once the integrated signals without DC components is derived (Figure 2.17b), the number of samples between the peaks of the fundamental frequencies of the signals gives the phase shift ( supposing the number of samples for the whole period equals 360 degrees). The fundamental frequency can for example be obtained by a FFT; this work's post-processing algorithm derives the fundamental with the matlab "sum of sines" function which is closely related to the discrete Fourier transform.

An alternative method derives the PF from the transformed $dq$ voltage and current. The $dq$ transformation yields the same angle between $\vec{u}_{dq}$ and $\vec{i}_{dq}$ as between the terminal voltages and currents. Therefore, cosinus of the absolute value of a subtraction between the voltage and current angle in regard to the $d$ axis in the $dq$ frame gives the power factor

$$\cos(\phi) = \cos\left(\overline{\theta^u_{dq} - \theta^i_{dq}}\right) \tag{2.56}$$

Since the current and voltage always exist in the second or third quadrant in the $dq$ frame (the current is always in the third, but the voltage can exist in the forth if the negative $d$ current gives rise to a flux which is greater then the permanent magnet flux), the current and voltage angle in respect to the $d$ axis are given by

$$\theta^u_{dq} = \tan^{-1}\left(\frac{u_q}{u_d}\right) + \pi$$
$$\theta^i_{dq} = \tan^{-1}\left(\frac{i_q}{i_d}\right) + \pi$$

The benefit of this method compared to the procedure which derives the PF directly from the phase voltages and currents is that $\vec{i}_{dq}$ stays constant throughout the tests. Furthermore, the voltage changes fairly linearly with speed. This makes it easier to filter the signals, and the post-processing algorithm becomes less complicated.

### 2.4.5 Loss separation

The losses in a PMSM can be divided up in three main parts

1. **Resistive stator winding losses.** These losses are practically assumed to be independent of frequency, even though this is not true since the proximity and the skin effect affect the resistance. The resistivity of the conductor is also highly temperature dependent, which leads to a change in the losses when the windings heat up.

2. **Losses in the core.** The core losses are often divided up in three categories: hysteresis, eddy current and excess losses [37]. Hysteresis losses occur because of the non-linearity between the current in the winding and the flux density in the core; the magnetization and demagnetization of the core yield different relationships between the magnetic field strength (proportional to the current) and the magnetic flux density. This creates energy demanding hysteresis loops which manifest as losses in the machine. The hysteresis losses are assumed to be proportional to the frequency of the flux density.

   The eddy current losses are due to induction in the core alloy which the time varying magnetic flux density gives rise to. The core is usually laminated to limit this phenomenon, but when the frequency is high the eddy currents still cause considerable losses in the machine. These losses are proportional to the square of the frequency.

   The excess losses occur when the flux density which the stator

current and permanent magnets give rise to interacts with the highly inhomogeneous flux created from the induced eddy currents [37]. The losses are approximately proportional to the frequency powered by one point five in most core materials.

3. **Mechanical and windage losses.** The mechanical and windage losses consists of bearing and air friction and depend on the properties of the bearings, the shape of the rotor and the air-gap length. Approximately, the bearing friction losses depends linearly on the frequency while the windage losses have a cubic relationship to it.

A first step in the loss separation process is to divide the losses which brakes the rotor of the machine with the losses that are due to the stator current. The losses which brake the machine give rise to a loss torque, which may be derived by subtracting the mean air-gap torque ($T_{ag}^{m}$) from the rotor shaft torque (if flux leakage is neglected). This loss torque includes all speed dependent losses in the machine. Since the flux, currents, acceleration and moment of inertia of the rotor axis are known, the loss torque can be derived directly from the DTM measurements

$$T_{loss} = \left( i_q^s \psi_d^{(i_d^s, i_q^s)} - i_d^s \psi_q^{(i_d^s, i_q^s)} \right) - J \frac{d\omega}{dt} \tag{2.57}$$

Supposing that the windage losses are negligible, the power losses which brake the machine can be approximated by

$$P_{T_{loss}} = K_f \omega_m + K_h p \omega_m + K_{exc} p \omega_m^{1.5} + K_e p \omega_m^2 = T_{loss} \omega_m \tag{2.58}$$

where $p$ is the number of pole pairs, $K_f$ is the friction loss coefficient and $K_h$, $K_{exc}$ and $K_e$ are iron loss coefficients. Since the power is the torque times the speed, the expression for the loss torque becomes

$$T_{loss} = K_f + K_h p + K_{exc} p \sqrt{\omega_m} + K_e p \omega_m \tag{2.59}$$

The equation above shows that the friction and the hysteresis losses introduce a constant braking force on the rotor axis, while the excess and eddy current forces increase with speed. The expression does not allow for a separation between the friction and the hysteresis losses. Even so, it is possible to find the eddy current and excess loss coefficients if the evolution of the loss torque is examined.

Ideally, the loss torque includes all losses except for the losses in the copper. This is not entirely true since the resistance in the stator windings is frequency dependent. With that being said, if the coils are made up of litz wire, the skin and proximity effects are attenuated to the point where the frequency dependence can be neglected. In that case, the resistance introduces a constant loss which easily can be separated from the speed-dependent losses.

### The retardation method

A complementing measurement procedure which can be combined fairly easily with the DTM without the need to introduce more equipment, is the retardation method. The IEEE standard for testing synchronous machines suggests this method to find the rotor iron and friction losses. This is the measurement procedure: The machine is accelerated up to base speed whereupon the phases are disconnected from the converter. After the disconnection, the machine decelerates due to losses. If the rotor position is measured during the procedure and the moment of inertia of the rotor shaft is known, the losses can be derived from the equation of the rotor shaft torque. Since the electromagnetic torque and the load torque are zero, the change of speed and the moment of inertia give the loss torque directly.

Since the magnetization cannot be turned of in a PMSM, it is not easy to separate the iron losses that are induced by the permanent magnet flux from the friction losses. The only way to get around this problem is to first test the machine with a rotor without permanent magnets, and then exchange it for the PM rotor. Even so, the retardation test still gives valuable information of the open circuit characteristics of the

machine. It can be specially interesting to compare the open-circuit loss torque with the loss torque that occur during loading. This can give a clue on how the stator current flux interacts with the flux from the permanent magnets.

#### Conclusions

The loss separation procedure of the DTM is still under development, and the ideas which this section presents have not yet been evaluated. Even so, The DTM has potential to be useful for these kind of purposes, in addition to providing flux and torque characteristics of a machine.

## 2.5 Measurement considerations

This section discusses different measurement considerations from the magnetic model derivation point of view. Even so, much of the information is also valid for the efficiency measurements and loss separation. A more elaborate discussion regarding the data acquisition and treatment for the efficiency measurements is a topic for future research.

### 2.5.1 data acquisition

#### Rotor position

A high precision rotor angular position measurement is important for accurate DTM results. Hypothetically, the position is not needed for the derivation of the flux if the angular speed of the rotor and the voltages in the $dq$ frame are available. However, the $dq$ transformations in the control system still need accurate rotor position measurements to provide reliable variables. As it is easier to process data off-line, both the frequency – which is the derivative of the position – and the $dq$

currents and voltages are derived from the measured position in the scheme which this thesis presents.

Most high accuracy and cost effective angular position sensors give two sinus waves in quadrature relationship to provide information about the rotor position [38]. The position sensor of the test machine which chapter 3 presents is a resolver, which, given an excitation signal, provides the sine waves with information about the position. In addition to the rotor position information, the signals from the sensor also carry harmonics with the same frequency as the excitation. The resolver signals must therefor be demodulated to obtain the rotor position. Throughout the experiments in this work, the demodulation process underwent with the assumption that the high frequency components of the resolver signals and the excitation signal were in phase. Under such circumstance, the excitation signal can be used directly in the demodulating process [39], [40]. In the procedure that was used during this work, the demodulation algorithm finds the peaks of the resolver signal high frequency component; mr Yury Loayza designed and implemented the code for the demodulation.

The process of deriving the position after the demodulation is straight forward. Supposing ideal steady-state resolver signals, they can be expressed mathematically as

$$u_d^{\text{res}} = |u| \cos\theta \sin\omega_{\text{ex}} t \tag{2.60}$$

$$u_q^{\text{res}} = |u| \sin\theta \sin\omega_{\text{ex}} t \tag{2.61}$$

where $\theta$ is the rotor position and $\sin\omega_{\text{ex}} t$ is the high frequency excitation component. The demodulation process removes the high frequency component, and the expressions for the demodulated resolver signals become

$$u_d^{\text{res}} = |u| \cos\theta \tag{2.62}$$

$$u_q^{\text{res}} = |u| \sin\theta \tag{2.63}$$

The rotor position can now be directly obtained with the arcus tangens

function

$$\theta = \arctan \frac{u_q^{\text{res}}}{u_d^{\text{res}}} \tag{2.64}$$

To avoid zero division problems with the expression above, theta may be derived with the coordinate rotational digital computer (CORDIC) algorithm [41]. The CORDIC algorithm iterates through different angles by rotating the measured vector ($\cos\theta + j\sin\theta$) back and forth until the argument is approximately zero (the accuracy of the procedure is related to the number of iterations the algorithm performs). The actual position can be derived since the algorithm knows how many degrees the measured vector rotates throughout the procedure. The algorithm is suitable to implement on field programmable gate arrays (FPGAs) and derived the rotor position during the experiments.

A control loop which suppresses the error of the angle gives an alternative way to obtain the rotor position. The algorithm derives the cosinus and sinus of the estimated angle, whereupon (2.62) is multiplied by the estimated sinus, and (2.63) is multiplied with the estimated cosinus. A subtraction of the two multiplications together with trigonometric operations yield an estimation of the error. The error is then suppressed by a loop similar to a phase locked loop. This procedure was not used for the experiments presented in chapter 4, but many papers recommend it for a more reliable and stable angle derivation [39], [40], [42], [43], [44].

### Voltage

The converter phase voltage is maybe the most challenging DTM variable to obtain. The literature presents a couple of solutions: Analog integrator circuit methods integrate one switching period and thus provide the quasi-instantaneous mean value of the voltage [45], [46], [47]. The procedures give accurate results, but the circuits need time-consuming manual tuning, and the value of the passive components tend to drift

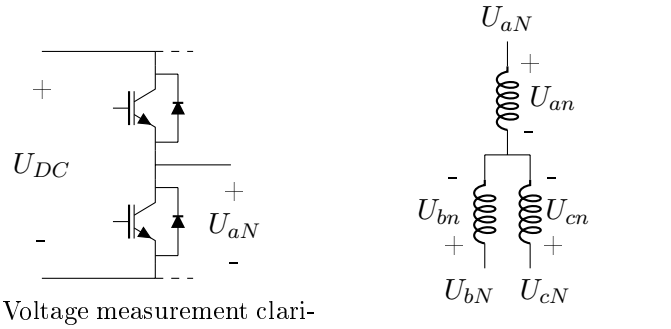


(a) Voltage measurement clarification

(b) Simple equivalent model

Figure 2.18: Converter and machine voltages defined

with temperature. Digital integration also provides high accuracy measurements: High speed high accuracy analog to digital (A/D) converters obtain the instantaneous voltages and a digital circuit, typically a field programmable gate array, performs the integration [48]. The procedure avoids the manual tuning and temperature dependence of the analog circuits, but the high speed, high precision A/D converters are costly. A third phase voltage estimation strategy is to use the current controller reference value as DTM data. The switching dead-time, the rise an fall time, and the voltage drop over the semi-conductors in the converter must be taken into account for accurate estimations [49],[50],[51]. The strategies are designed for a constant switching frequency, and they do not work with the current control strategy of the DTM magnetic model derivation.

The strategy which was used during the measurements in this project obtains the voltages by controlling the voltage level in between the converter leg's transistors while at the same time keeping track of the DC link voltage. The method has been evaluated before, but without taking voltage drops over the converter semiconductors into account [52]. Figure 2.18a helps to describe the strategy: Differential probes measure $V_{aN}$, $V_{bN}$ and $V_{cN}$, which are the phase to DC link neutral voltages. Since high speed and high accuracy analog to digital converters are costly, the three probes are connected to a very high speed digital inputs; the measurements provide information regarding the state of

each phase leg.

While the DAQ system obtains information regarding the phase leg states, a sensor together with an high accuracy but low speed analog to digital (A/D) converter collects DC link voltage measurements. The sampling speed of the A/D converter can be slow as the change of the dc-link voltage is limited by the DC link capacitor. Since $V_N$ is approximately $V_{DC}$ when the upper transistor conducts, and zero if not, a multiplication between the state of a phase leg and $V_{dc}$ gives an approximation of $V_N$. The differential probes measure the actual switching of the transistors and the necessary switching dead-times, when both transistors in one leg are turned of, are therefore taken into account. On the other hand, the voltage drop over the transistors and free-wheeling diodes still introduce errors in the measurements. The expressions for the converter leg voltage over one period without taking the semiconductor voltage drops into account become

$$U_N = \frac{1}{N} \sum_{k=1}^{N} \delta(k) \cdot U_{dc}(k) \tag{2.65}$$

where $\delta$ is the state of the converter legs. To reduce the transistor and diode voltage drop errors, they are added or subtracted from $U_N$: If the upper transistor conducts and the phase current is positive, the voltage drop over the transistor is subtracted from $U_N$. If, on the other hand, the current is negative, the voltage drop over diode is added to $U_N$. When the lower transistor conducts, the voltage drop of the diode is added if the current is positive, and the transistor voltage drop is subtracted if the current is negative. This error reduction demands that the on state voltage drop over the semi-conductors are known. As the voltage drops are functions of the current, this compensation procedure is not trivial to perform. The voltage drops can be expressed mathematically as

$$U_{drop}(x) = \begin{cases} +U_{trans}, & i < 0,\ \delta = 1 \\ +U_{diode}, & i > 0,\ \delta = 1 \\ -U_{trans}, & i < 0,\ \delta = 0 \\ -U_{diode}, & i > 0,\ \delta = 0 \end{cases}$$

and (2.5.1) together with (2.65) yield a refined expression for the converter leg voltage

$$U_N = \frac{1}{N} \sum_{k=1}^{N} \delta(k) \cdot U_{dc}(k) - U_{drop}(k) \tag{2.66}$$

Figure 2.18b shows a simplified equivalent circuit of the machine. Once $U_{aN}$, $U_{bN}$ and $U_{cN}$ are obtained, Kirchoffs voltage law (KVL) yield the phase voltages in regard to the Y connected machine neutral

$$U_{an} = \frac{2}{3}\left(U_{aN} - \frac{U_{bN}}{2} - \frac{U_{cN}}{2}\right) \tag{2.67}$$

$$U_{bn} = \frac{2}{3}\left(U_{bN} - \frac{U_{cN}}{2} - \frac{U_{aN}}{2}\right) \tag{2.68}$$

$$U_{cn} = \frac{2}{3}\left(U_{cN} - \frac{U_{aN}}{2} - \frac{U_{bN}}{2}\right) \tag{2.69}$$

These are the voltages that are used to derive the linked magnetic flux in the magnetic model derivation.

### Current

The DTM demands high precision instantaneous current measurement to give good results. The IEEE standard for measurements in power circuits describes some approaches to obtain the current [53]. One of these

procedures uses Hall sensors, which measured the current throughout this work's experiments. The Hall sensor does not intervene directly with the current path. Instead, it is placed around the conductor, and the magnetic field which the current gives rise to induces a voltage in the sensor.

After the voltage is induced, an op-circuit amplifies the signal to suit the level of the analog to digital converters of the control system. The amplifier circuit is prone to introduce some level of offset, and a perfectly symmetric amplification of the three phases can not be taken for granted. The control system needs to compensate for these imperfections for good results; section 2.5.3 discusses this further.

### 2.5.2 Post-processing

The post-processing procedure after the measurement data is acquired is not part of the conceptual idea of the dynamic test method. With that being said, it may be interesting for the reader to get an idea of how the data can be processed to reach a satisfying result. This section shows an example of how measurement data can be processed, and also how the results presented in chapter 4 were derived.

#### Rotor position and electrical frequency

Figure 2.19a shows an example of measured rotor positions throughout a test cycle. The measurements span between minus pi and pi, where one period is two pi. To make it easier to process the data, the samples are stacked on top of each other (Figure 2.19c). This leads to a smooth curve which can be low-pass filtered to reduce noise of the obtained position. Figure 2.19d shows a zoomed in example where the measurements (the blue dots) are filtered (the red line).

The choice of low-pass filter algorithm for the position has a big influence of the outcome of the flux derivation: If the filter is to fast,

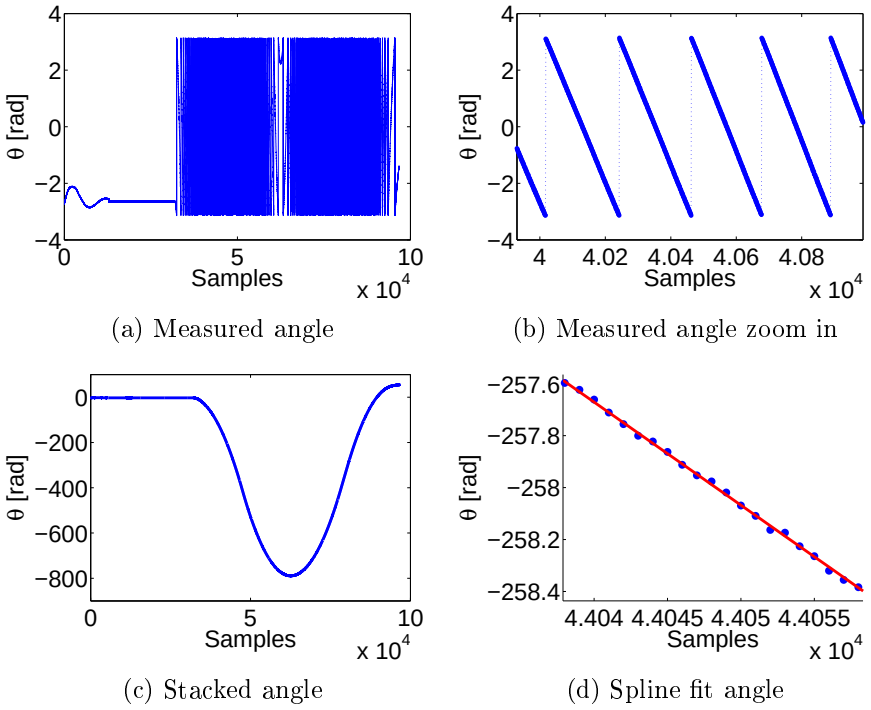


(a) Measured angle (b) Measured angle zoom in

(c) Stacked angle (d) Spline fit angle

Figure 2.19: Measured rotor position

the flickering in the position measurements leads to a big ripple in the frequency estimation. If, on the other hand, the filter is to slow, the low-pass filtered position will not follow the actual position when the rotational direction changes (this is where the position change the most, which also is the minimum point in Figure 2.19c). In the results which chapter 4 presents, a spline interpolation filters the signal.

The spline interpolation works well as it follows the measured position with a low degree polynomial which is robust against high frequency noise in the signal. The spline is divided up in several segments, and an interpolation is done within each. For the results that chapter 4, the matlab function splinefit by mr. Jonas Lundgren interpolated the measured rotor position data.

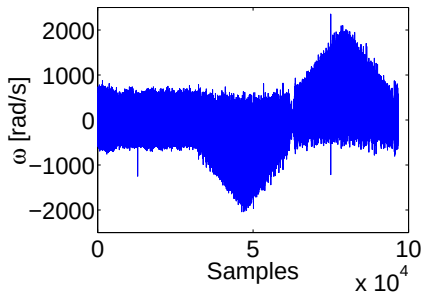


(a) Angular frequency from raw angle

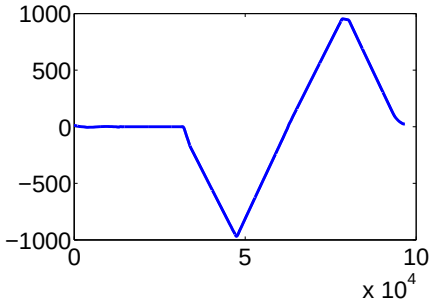


(b) Angular frequency from spline fitted angle

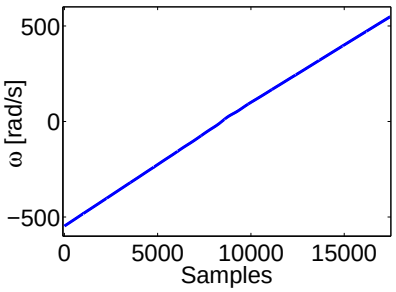


(c) Measurements used for the magnetic model derivation

Figure 2.20: Speed derivation

To show how important it is to low-pass filter the position, Figure 2.20a presents the angular frequency derived from the non-filtered position, while Figure 2.20b presents the frequency estimated from the filtered signal. The derivative of the raw position estimation has a very big ripple due to the noise of the raw measurements while 2.20b shows a smooth curve. Figure 2.20c displays the cropped speed range, which is the data the magnetic model derivation algorithm uses.

### Voltage

Figure 2.21a shows measurements of $U_{aN}$ (see Figure 2.18) throughout a test sequence. The harmonic content of the voltage is very high.

Furthermore, the amplitude varies throughout the test sequence. The harmonics are – apart from a non-sinusoidal induced voltage – due to the variable frequency of the current controller. The variations of the amplitude are due to the rotating converter that supplies the test rig with the DC-link voltage. This is an unwanted phenomenon, but it is specific for the setup that was used throughout these tests, and is therefore not an intrinsic behavior of the method itself. The raw measurements $U_{aN}$, $U_{bN}$ and $U_{cN}$, together with (2.67), (2.68) and (2.69), yield $U_{an}$, $U_{bn}$ and $U_{cn}$. Figure 2.21b shows that high harmonic content remains after the derivation.

$U_{an}$, $U_{bn}$ and $U_{cn}$ remain unfiltered when they, together with (2.1), (2.2) and the raw measurements of the rotor angle, give the $dq$ voltages. Figure 2.22a shows that the harmonic content of the resulting $d$ voltage is, as expected, very high; the same is true for the $q$ voltage. Figure 2.22a also displays another interesting phenomenon: The change over time, if the harmonics are disregarded, is much slower compared to the $U_N$ and $U_n$ voltages. Because of this, a low-pass filter works better on the $dq$ voltages than the phase voltages, as the time constant can be lower without affecting the fundamental component of the signals.

Figure 2.22b shows the $d$ voltage after it is low-pass filtered with same spline algorithm that filters the rotor position measurements. The voltage changes nearly linearly with time, which is expected as the induced voltage is linearly dependent on the electrical frequency.

### Current

The post-processing of the current is straight forward. The obtained rotor position together with the $dq$ transformations yield the current in rotor coordinates. Since the currents play no explicit role in the flux derivation, their function is to show that the measurements are correct. If the currents are noisy, they may be filtered to control that the quasi-instantaneous values are correct.

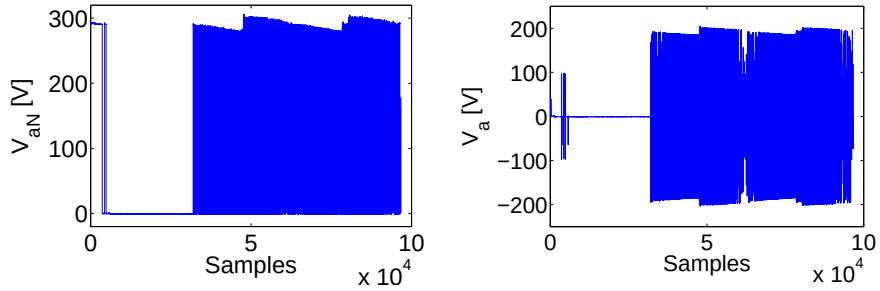


(a) Measured $U_{aN}$ (b) Derived $U_{an}$

Figure 2.21: Raw converter voltage and machine phase voltage measurements

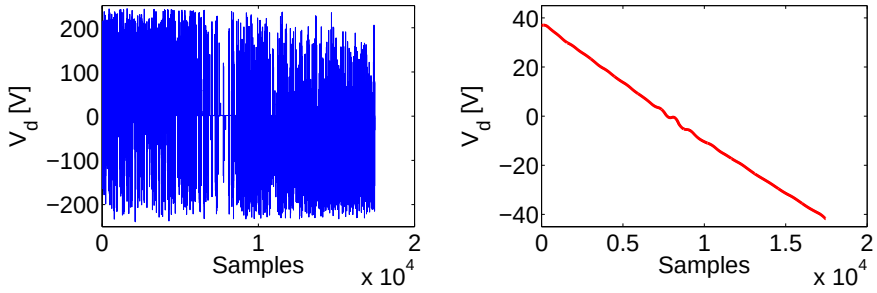


(a) Raw $d$ voltage (b) filtered $d$ voltage

Figure 2.22: $d$ voltage

### 2.5.3 Measurement errors

#### Position measurements

Errors in the rotor position estimation when performing dynamic tests can have great influence on the end results. The errors can manifest as a ripple and/or an offset. Offset errors are the most severe as they introduce a shift in the $dq$ reference frame. Figure 2.23 shows a possible scenario when an offset error is present. The shift in angle makes the transformed $dq$ currents differ from the reference currents, and the flux

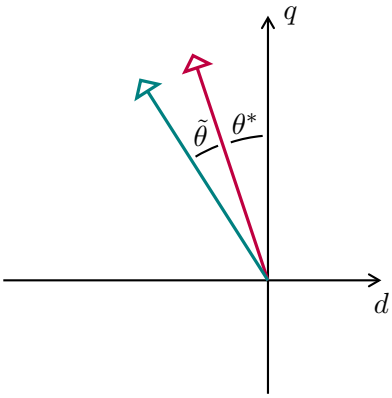


Figure 2.23: Shift in the $dq$ coordinates due to offset in the resolver measurements. $\theta^*$ is the reference angle and $\tilde{\theta}$ is the error

maps are thus shifted. The oscillating errors may inflict torque ripple, but since many measurements are obtained and averaged over a DTM test sequence, they do not affect the results in a significant way. The measurement procedure can be divided up in three stages which can introduce errors:

1. There exist disturbances in the signals generated by the resolver. The resolver signals always contain noise and asymmetry to a certain extent. This may have a non-negligible effect on the demodulation process and position measurement if the imperfections are too prominent. The most common resolver signal errors can be divided up into six categories, where two are of great significance to the DTM [42]:

    a) The two resolver signals are not in a perfect quadrature. This imposes both an oscillating error and an offset error in the position according to $\epsilon = -\frac{\beta}{2}(1 - \cos 2\theta)$, where $\beta$ is the phase shift which makes the signals deviate from a quadrature relationship, and $\theta$ is the rotor position. A correction process of this type of errors is described in [43].

    b) The excitation signal and the high frequency component of

the returning resolver signals are not in perfect synchronization. This error is unavoidable due to the resistance of the resolver windings. The phase shift introduces an error which is dependent on the change of the resolver angle according to $\epsilon = \frac{\dot{\theta}}{\omega}\delta$, where $\omega$ is the electrical radial frequency and $\delta$ is the excitation signal phase shift. A demodulating procedure that cancels this error is presented in [44].

2. The demodulation process together with the angle derivation from the demodulated signals introduce errors due to noise sensitivity. These errors introduce ripple in the position estimation, but does not inflict a permanent offset, and they do not create to much complications for the DTM.

3. The resolver can be poorly calibrated, which means that the $d$-axis is not perfectly aligned with the permanent magnet flux. This introduces a constant offset in the angle which, as mentioned before, affects the results of the DTM.

Since an error in the angle imposes a rotation of the reference frame, the impact of it depends on the characteristics of the machine, and a quantitative estimation of how much a specific error affects the test results is therefore impossible to make.

### Voltage

The voltage is the only DTM variable which does not take an active part in the control system. The testing performance is therefor unaffected by an error in the voltage. With that being said, errors in the measurements still have an impact on the magnetic model and efficiency derivation. The possible reasons for measurement errors –neglecting sources such as rise/fall time of the semi-conductor devices and voltage flickering/over shoots, which are impossible to detect with the used method– may be divided up in three categories:

1. The differential probes or the digital sensors fail. When this happens, the converter leg measurements are lost and the tests must be remade.

2. The DC voltage measurements are badly tuned. Since the DTM does not affect the test procedure, an estimation of the effect of an error in the DC voltage measurement can be reached in the post-processing. Supposing an error factor $\alpha_e$, and neglecting the voltage drop over the converter components, the converter leg phase voltages become

$$\tilde{U_N} = \alpha_e U_{dc} \delta_N = \alpha U_N \tag{2.70}$$

$U_N$ together with (2.67)-(2.69) yield

$$\tilde{U_n} = \alpha_e U_n \tag{2.71}$$

The $dq$ transformations are linearly dependent on the amplitude of the variables that are being transformed if they are symmetric. The expression for the $dq$ voltages thus becomes

$$\tilde{u_{dq}} = \alpha_e u_{dq} \tag{2.72}$$

Finally, the derived voltages together with (2.22) and (2.23) show that

$$\tilde{\psi_{dq}} = \alpha_e \psi_{dq} \tag{2.73}$$

This expression holds for both a gain and a offset error since the DC- link value is considered constant. If the DC-link voltage drops throughout the sequence, a gain error changes while an offset error remains the same. As long as the voltage drop is not severe, the

change of the gain error is very small and can be neglected, and (2.73) therefor holds.

3. The estimations of the voltage drops over the components in the converter are wrong. The errors are functions of both the state of the of the voltage legs and the sign of the currents. If the factor of the error is denoted $\beta_e$, the new expression for the converter leg voltage is expressed as

$$U_N = \frac{1}{N}\sum_{k=1}^{N} \alpha_e \cdot \delta(k) \cdot U_{dc}(k) - \beta_e(k) \cdot V_{drop}(k) \tag{2.74}$$

Note that $\alpha_e$ is independent of the position sample of the integration while $\beta_e$ – as can be seen in (2.5.1) – is. This makes it impossible to estimate the influence of $\beta_e$ in the post processing. With that being said, the influence of $\beta$ is much less than $\alpha_e$, and has very little influence on the end result of the measurements.

### Current

In contrast to the voltages, errors in the current measurements affect the on-line performance of the DTM testing process directly. There are two common errors which can occur during the measurement procedure [54]:

1. One or many of the sensors, measurement circuits and/or A/D converters imposes an offset on the provided signals.

2. The gains of one or more of the signals are wrong.

Figure 2.24 shows what happens when the different errors are imposed on one phase of a perfectly symmetric three phase system. An offset error adds an oscillating component to the $dq$ currents. As the controller tries to keep the $d$ and $q$ current constant, it makes the amplitude of

one of the phase currents oscillate. This imposes a torque ripple on the machine.

An asymmetric gain error both imposes an oscillating signal, and gives rise to an offset in the currents in the rotor reference frame. Since the controller tries to keep the measured current at the reference value, the actual tested combination varies with time. Even more importantly, it oscillates around a rotor reference current which deviates from the one the control system aims to evaluate. This means that the flux maps that the algorithm derives apply to unknown current combinations which deviate from the intended. Caution should therefor be taken to adjust the gains of the currents in the control system to accurate values.

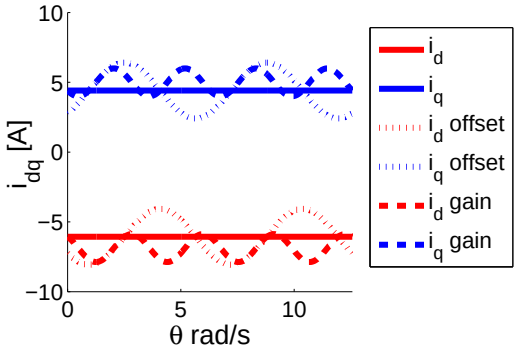


Figure 2.24: Influence of errors in the current measurements

# Chapter 3

# Experimental Setup

Figure 3.1 shows how the equipment was set up for the experimental tests. A central control and DAQ system controls the converter which drives the test machine. A resolver sensor provides the necessary information about the rotor's position. Hall sensors measure the currents, and voltage probes give the duty cycle of the phase voltages as described in chapter 2.

A DC machine driven mechanically by an asynchronous machine provides the voltage on the DC side of the converter. As the DC machine works both as a motor and as a generator, the DC link is able to absorb as well as provide electrical energy. This feature is, as mentioned in chapter 2, essential for the dynamic test method to work; an ordinary DC rectifier can therefor not be used for this method.

## 3.1 Control and DAQ unit

National instruments compact rio system (cRIO) was used to control the converter voltage and to gather data throughout the testing. The system includes a real-time system and a field programmable gate array (FPGA) together with an interface to a personal computer. In addition, integrated slots for in and out modules make it easy obtain data and to communicate with the outside world.

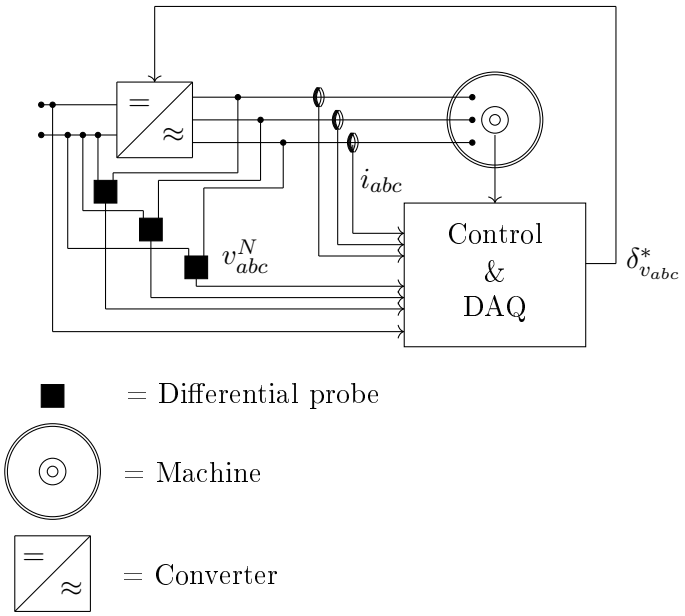


Figure 3.1: Experimental test setup

The FPGA part of the cRIO is a desirable platform for control and data collection due to its precise timing and true parallelism, but space and memory restriction limits the amount of code that can be executed on it. Functions which are in need of timing and speed performance, such as current control, were therefor implemented on the FPGA, while the control of the entire test sequence – which is less time critical – was implemented on the real-time part of the system. A first in first out (FIFO) communication sent the measurement data from the FPGA to the PC where it was stored for data post-processing.

## 3.2 Setup for constant speed tests

To compare the results form the dynamic test measurements with results from a more established test procedure, a setup was created for constant speed tests. Figure 3.2 shows the design of the setup. Com-

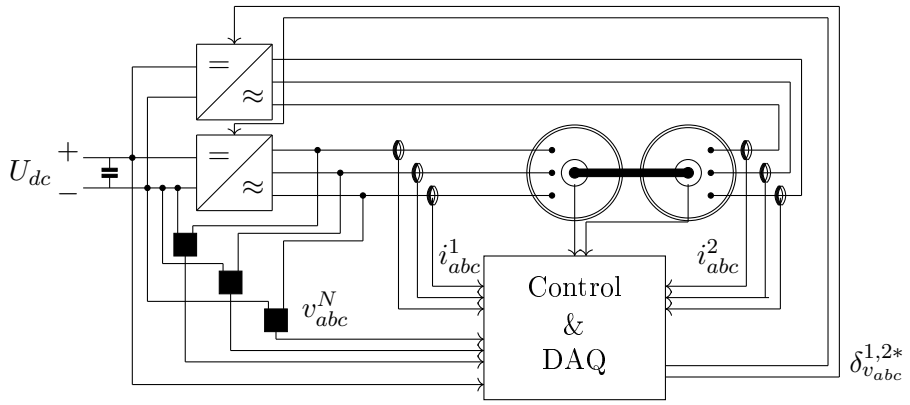


Figure 3.2: Experimental test setup for constant speed tests

pared to the dynamic test setup (Figure 3.1), an additional machine is introduced and connected mechanically to the test object. The machine works as a generator if the test object is tested as a motor, and as a motor if the test object is evaluated as a generator. A second converter controls the new machine.

Because of the new machine, the speed of the test object can be held constant independently of the torque it produces (supposing that the new machine is strong enough). In this works setup, the additional machine was very similar to the test object, which made it possible to perform the tests over a wide speed and torque range. Figure 3.3 shows how the test object and the second machine was assembled. There was also a torque sensor mounted in between the machines, but it was not used for the tests presented in this work.

## 3.3 Test object

Figure 3.4 shows the design of the test object. The machine is an eight pole permanent magnet machine with integrated magnets designed by Dr. Fransisco J. Márquez-Fernández for an electrical rear wheel drive unit. Due to the integrated magnets, the saliency of the machine (the

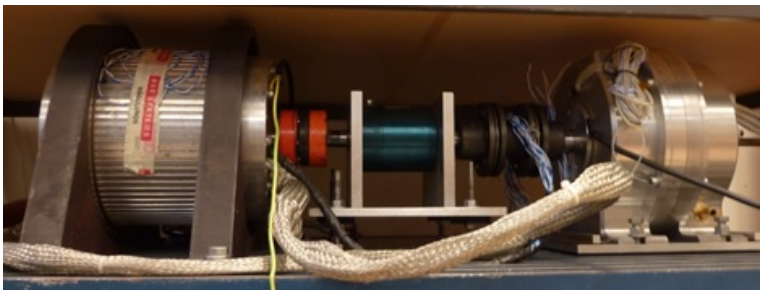

Figure 3.3: Setup for constant speed tests

difference of inductance in $d$ and $q$) is relatively high. The machine is designed for 20 kW continuous power with an overload capability of three times, and a maximum speed of 15000 rpm with a field weakening ratio of 1:5. More information regarding the design of the machine can be found in [55].

The machine features various integrated pt100 temperarure sensors mounted in different locations. The sensors give information about the winding, iron, and to a certain extent permanent magnet temperature. This information is valuable since material characteristics – such as the resistivity of the copper and magneto-motive force of the permanent magnets – change when losses heats up the machine. In this work, only the winding temperature sensor, denoted with blue circles in figure 3.4, was used; in a more excessive study it would be interesting to monitor the permanent magnet temperature also (this was not performed due to lack of time). A thorough investigation of the temperature properties of the machine is found in [56].

## 3.4 Equipment for rotor moment of inertia derivation

To be able to find the rotor moment of inertia three flywheels with different moment of inertia was custom made for the test object. In addition, a trifiliar pendulum was created to measure the moment of

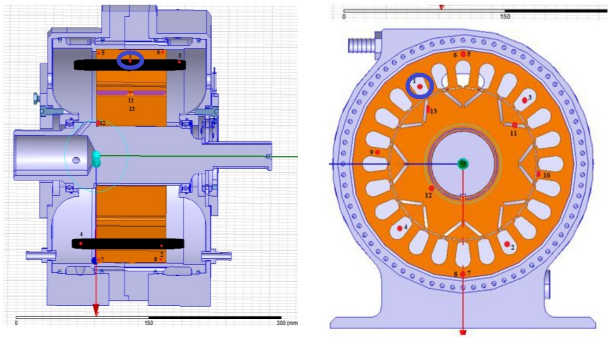

Figure 3.4: Placement of pt100 sensors. Taken from [56], with permission

inertia of the flywheels. The equipment that was used to derive the rotor moment of inertia is seen in figure 2.10 in chapter 2.

# Chapter 4

# Experimental Results

This chapter presents results from experimental tests performed with the dynamic test method. Since many experiments have been performed throughout the project, the current range of the results vary. Generally, the sections show the material in the same way that it is presented in publications, and a lot of the results in this chapter can therefore also be found elsewhere. The purpose of this chapter is first and foremost to string together the different parts and give a coherent overview of the results.

## 4.1 Magnetic Model identification

### 4.1.1 The magnetic model

Figure 4.1 shows the resulting flux maps from the DTM tests. The linked magnetic $d$ flux (Figure 4.1a) is about 0.125 Weber without field weakening current. A negative $d$ current gives rise to a flux which opposes the one from the permanent magnets, and the resulting $d$ flux linkage therefor decreases. When the negative $d$ current is big enough, it cancels out the flux from the permanent magnets entirely, which means that $\psi_d$ is zero, and torque is only generated due to the magnetic asymmetry of the rotor (reluctance torque).

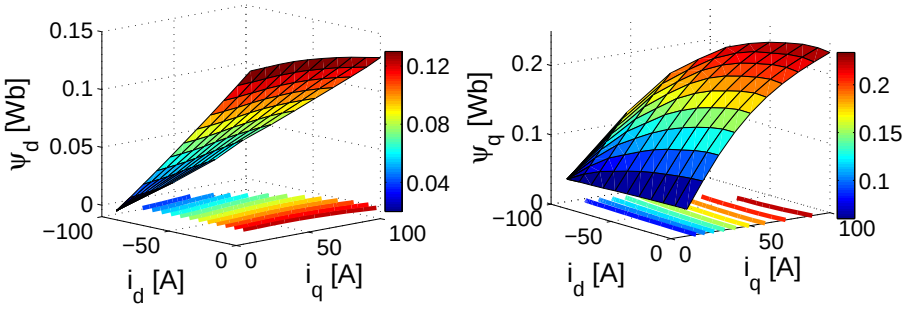


(a) $d$ flux (b) $q$ flux

Figure 4.1: Linked flux as functions of the $d$ and the $q$ currents

The estimated $q$ flux (figure 4.3b) is, in contrast to the $d$ flux in regard to the $d$ current, highly nonlinear in regard to the $q$ current. This is due saturation in the iron core. The nonlinear behavior makes it unfitting to express the relationship between the current and the flux as an inductance (as a matter of fact, this phenomenon is the reason why the magnetic model in this work is presented as flux maps and not as inductance maps).

### 4.1.2 Comparison with results from FEMM simulations

Figure 4.2 shows comparisons between results from a 2D FEM simulations on the machine and the results from the DTM. The $q$ flux results fit well (Figure 4.2b), while the DTM derives lower values than the simulation for the $d$ flux (Figure 4.2a). The reason for the discrepancy in the $d$ flux is not obvious, but possible reasons are a too low reluctance in the $d$ axis magnetic circuit in the FEMM model, that the magnetomotive force in the permanent magnets are modeled to high or that the simulations does not take the end-turn inductance of the machine into account. A more elaborate discussion regarding this phenomenon is found in [57].

The simulation model of the test object was already finished by Dr.

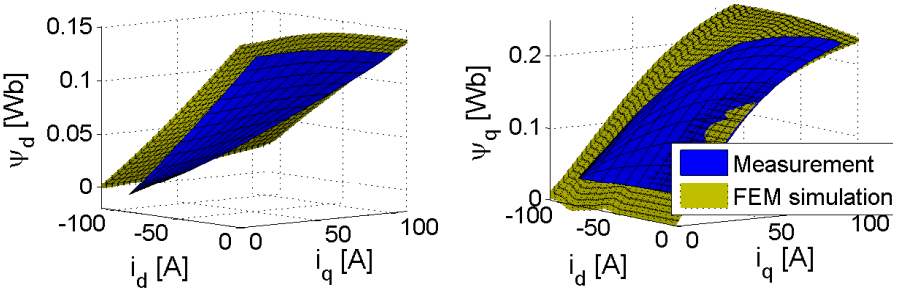


(a) $d$ flux (b) $q$ flux

Figure 4.2: Comparison between the magnetic flux linkage model derived by the dynamic test method (blue surface) and from FEMM simulations (yellow surface)

Francisco J. Marquez-Fernández before DTM experiments were conducted. All post-processing of the simulation results from the FEMM simulations was made in matlab; the post processing code was written as a joined effort of the IEA section in Lunds University. The author has not taken part of the writing of the code, but the code and model was used in consent with the creators. A detailed presentation and explanation of the simulations is found in [55].

### 4.1.3 Comparison with results from a constant speed method

In addition to the DTM tests, the test object was also evaluated with an established constant speed method (CSM) for comparison purposes. The test procedure of the CSM goes as follows: The speed of the test object is held constant by an additional brake machine while the desired current combination is applied. Many periods of the voltage and position are measured for each $dq$ current combination, and the resulting voltages in $dq$ are calculated from the measurements off-line. The derived voltages are very noisy due to harmonics in the induced voltage which the flux from the permanent magnets and the applied currents give rise to, and the results must be averaged over time for an accurate

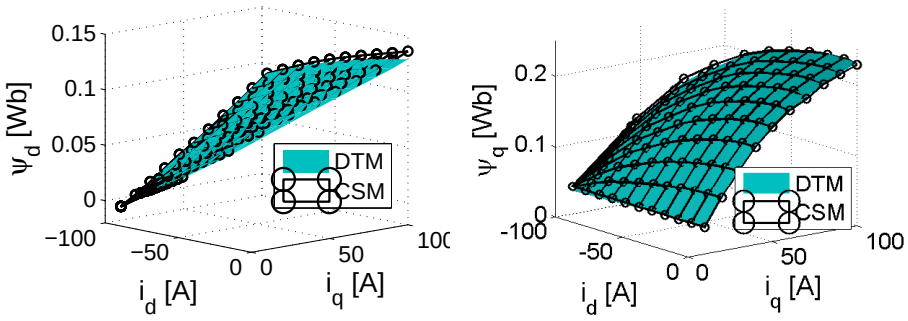


(a) $d$ flux (b) $q$ flux

Figure 4.3: Comparison between estimated flux from the constant speed method and the dynamic test method

flux estimation.

The theory of the CSM is based on the flux equations of the PMSM. Since the setup measures the voltages and currents, the only unknown variable in the equations is the stator resistance. This resistance is not trivial to estimate as it changes with temperature. In this case, it is measured with a high resolution multimeter at many temperatures. Since the winding temperature is monitored continuously throughout the tests, the change of resistance can be taken into account in the data post-processing procedure.

### Result comparisons

Figure 4.3 shows the magnetic flux linkage when the CSM derives the results compared with the DTM results. The results fit quite good, but the $d$ flux diverges with a big $q$ current and vice versa. The difference in the results can be explained by the change in flux linkage when the machine works in motor operation compared with generator operation (the difference occurs due to core losses, as explained in chapter 2). Since the results from the CSM is derived when the machine works as a motor, while the DTM results are obtained from measurements when

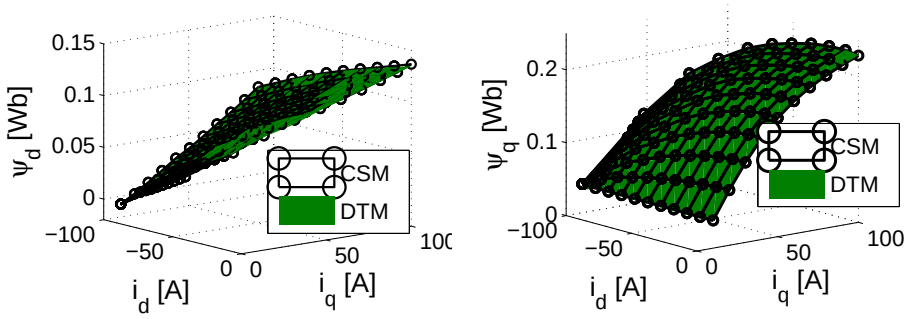


(a) $d$ flux (b) $q$ flux

Figure 4.4: Comparison between estimated flux from the constant speed method and the dynamic test method using measurements only from the motor part of the sequence

the machine works both as a generator and motor, a small difference is expected.

To make a fairer comparison, new maps are obtained from the DTM using only measurements from when the machine works in motor operation (when the machine accelerates). A rewrite of the PMSM voltage equations ((2.16) and (2.17)) yields the linked flux from the measurements. Figure 4.4 shows a comparison of the new DTM flux maps together with the results from the CSM. The results fits almost perfectly; there still exists a small offset in the $q$ flux when the $q$ current is small, but as figure 4.4b shows, it is marginal.

It should be mentioned that the results point towards an unrealistically big difference in the flux linkage when the machine works in motor operation compared with generator operation. Chapter 5 discusses this phenomenon further.

#### Temperature comparison

Figure 4.5 shows $d$ flux linkage results from the DTM and CSM measurements at two different stator winding temperatures. The same stator winding resistance value is used for both temperatures. The results from the dynamic measurements (figure 4.5a) shows an almost constant offset between the flux lines when the winding temperature differ around 35 degrees Celsius – the warmer machine links slightly less flux than the cooler. With higher $q$ currents than around 70 Amperes, the flux lines start to diverge. A possible reason for the constant offset is warmer magnets which leads to less flux density. The reason for the diversion at higher $q$ currents is unknown. Looking at the results from the CSM, the flux lines from the two temperatures are tilted slightly different (figure 4.5b). This is explained by (2.16): A too low resistance value leads to an overestimation of the flux. The phenomenon is especially apparent for big $q$ currents, where the results make you believe that a hotter machine links more flux than a cooler.

Figure 4.6 shows estimations of the $q$ flux. The results from the DTM are approximately the same independently of winding temperature (figure 4.6a). This is true except for when the $q$ current is very high, where – just as with the $d$ flux (figure 4.5a) – the hot machine links slightly less flux than the cold. The CSM results (Figure 4.6b) diverge when the $d$ current is high. This is due to the resistive voltage drop in (2.17), which, when a too small value is used, leads to a too high flux estimation.

### 4.1.4 Winding temperature development

If the DTM results should be independent resistive voltage drop, the winding resistance, and hence also the winding temperature, cannot change much during one test cycle. Figure 4.7 shows the change in the resistance in a resistance thermometer (PT100) which is mounted on a phase winding. The current combination $i_d^s = -100\text{A}$ and $i_q^s = 10\text{A}$ is chosen for the test as it gives the least torque for the most current; this is the worse case scenario in terms of heating of the windings during

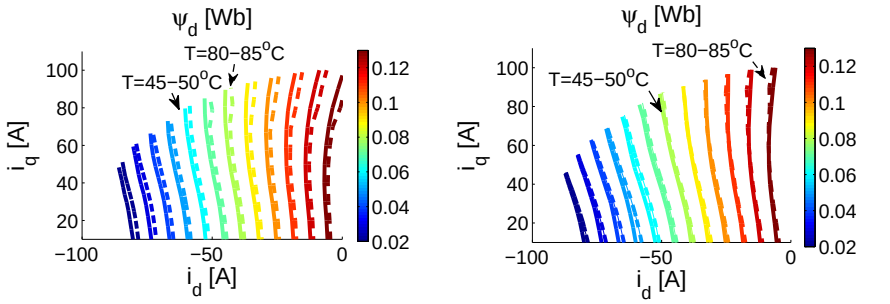


(a) Dynamic test method results (b) Constant speed method results

Figure 4.5: *d* Flux estimation from the dynamic method and the constant speed method at two different temperatures. The stator resistance value is assumed to be constant

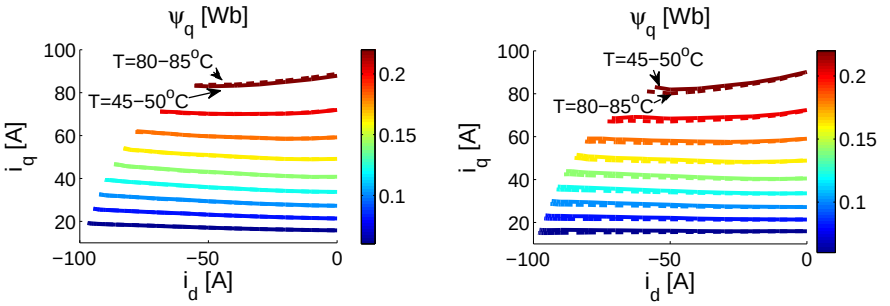


(a) Dynamic test method results (b) Constant speed method results

Figure 4.6: *q* Flux estimation from the dynamic method and the constant speed method at two different temperatures. The stator resistance value is assumed to be constant

one test cycle. The temperature change in the PT100 is approximately 0.15 Ω, which translates into 0.4$^o$C. The change is negligible and the assumption that the winding resistance remains constant during the test cycle is therefore considered correct (a notation here is that the PT100 is mounted on the side of the winding while the hot spot is in the center. In this case, the change is so small that the assumption is still considered safe).

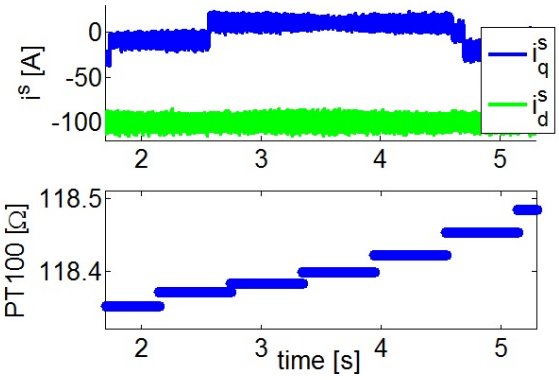


Figure 4.7: Resistance progression of winding temperature sensor during one test cycle

## 4.2 Torque derivation

### 4.2.1 From the flux and the currents (The air-gap torque)

Figure 4.8 shows the mean value of the motor and the generator torque ($T_{ag}^{m}$) of the machine calculated from the measured current and the estimated flux ($T_{ag}$). The torque increases with both a negative $d$ current and a positive $q$ current. There are two reasons why the torque increases with the currents: Firstly, the magnetic flux from the permanent magnets (which is aligned with the $d$ axis) interacts with the flux which the $q$ current give rise to. This can also be explained by the Lorentz law, which states that a force is created when a electric charge (which in this case is the currents that flows in the stator windings) interacts with a perpendicular magnetic field (which is the flux from the permanent magnets).

The second reason for torque generation is the different reluctance paths of the rotor which the interior permanent magnets – which have a much lower permeability than iron – give rise to. As the magnetic flux strives to flow through the path with minimal reluctance it creates a force to

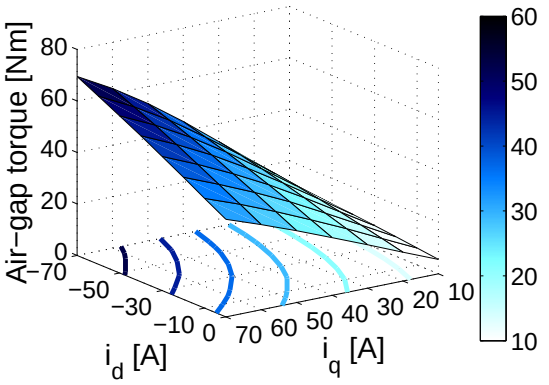


Figure 4.8: Torque results ($T_{ag}^{m}$) derived from the linked flux and the currents

align the rotors $q$ axis with the flux created from the stator windings.

### 4.2.2 From the acceleration and the moment of inertia (rotor shaft torque)

#### Estimation of flywheel and rotor moment of inertia

Calculations of the rotor shaft torque require information about the rotor shaft moment of inertia of the test object. In this case, the flywheel and pendulum method which chapter 2 presents provides the moment of inertia data. Table 4.1 shows the results of the three flywheel's moments of inertia from the pendulum measurements. The results seam reasonable with the weight and the geometries of the flywheels in mind: The inertia is linearly dependent on the mass, but has a more complicated relationship to the geometry. Since the parts close to the center of the flywheels are not equal in the three cases, it is expected that the results are not linearly dependent on the mass. On the other hand, since the geometries are similar, a big correlation between the mass and the moment inertia can still be found.

Table 4.1: Moment of inertia of flywheels

| Moment of inertia of flywheels | | | |
|---|---|---|---|
| Fly-wheel | Mass $[kg]$ | $\tau$ $[s]$ | J $[kg \cdot m^2]$ |
| 1 | 2.535 | 0.7635 | 0.0097 |
| 2 | 5.585 | 0.8183 | 0.0268 |
| 3 | 9.600 | 0.8105 | 0.0457 |

Table 4.2 shows the results of the extrapolated rotor moment of inertia values when 42 different torques was applied to the rotor shaft, and (4.1) and (4.2) show the mean value and the standard deviation of the results, respectively. The standard deviation is considered low enough to confide in the mean value of the moment of inertia.

Table 4.2: Extrapolated values of moment of inertia of the rotor

| | | | | | |
|---|---|---|---|---|---|
| -0.0206 | -0.0207 | -0.0209 | -0.0207 | -0.0209 | -0.0207 |
| -0.0211 | -0.0208 | -0.0211 | -0.0210 | -0.0210 | -0.0208 |
| -0.0206 | -0.0209 | -0.0210 | -0.0210 | -0.0211 | -0.0211 |
| -0.0206 | -0.0213 | -0.0207 | -0.0210 | -0.0205 | -0.0208 |
| -0.0214 | -0.0208 | -0.0209 | -0.0210 | -0.0210 | -0.0207 |
| -0.0198 | -0.0211 | -0.0212 | -0.0205 | -0.0216 | -0.0207 |
| -0.0216 | -0.0217 | -0.0218 | -0.0204 | -0.0209 | -0.0210 |

$$\overline{J_r} = 0.0209 \ [\mathrm{kg} \cdot \mathrm{m}^2] \tag{4.1}$$

$$\sigma_r = 0.00037 \ [\mathrm{kg} \cdot \mathrm{m}^2] \tag{4.2}$$

### Measurement results

Figure 4.9 shows the results of the mean value of the motor and generator torque ($T_{ag}^m$) estimations from the acceleration and moment of inertia measurements. The results are very similar to the torque estimations from the voltages and currents (Figure 4.8). The next section presents a more detailed comparison between the two ways to derive

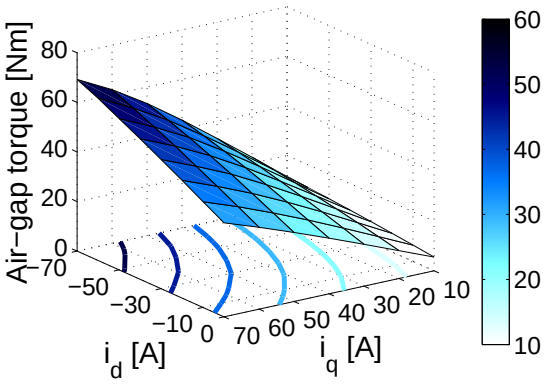


Figure 4.9: Torque results ($T_{ag}^{m}$) derived from the acceleration and the rotor shaft moment of inertia

the torques of the machine, together with a consistency analysis of the results.

### 4.2.3 Consistency analysis of the torque measurements

#### Deriving the torque with four different of moment of inertia on the rotor axis

For the DTM to be a reliable way to measure torque, the inertia of the rotor axis should not affect the results significantly. Tests were therefor performed without any flywheel, and with three different flywheels – the same flywheels which were used for the rotor shaft moment of inertia derivation – installed on the shaft, consecutively, to compare the results.

Table 4.3 shows the absolute standard deviation between the four measurements from each current combination. The deviation is calculated by

(a) Torque derived from the currents and voltages for each current combination

| $i_{sd} \backslash i_{sq}$ [A] | 10 | 20 | 30 | 40 | 50 | 60 | 70 |
|---|---|---|---|---|---|---|---|
| 0 | 0.0286 | 0.0500 | 0.0537 | 0.0886 | 0.0901 | 0.0932 | 0.0781 |
| -10 | 0.0152 | 0.0463 | 0.0419 | 0.0797 | 0.0127 | 0.1061 | 0.1342 |
| -20 | 0.0063 | 0.0241 | 0.0404 | 0.0769 | 0.0530 | 0.1253 | 0.0698 |
| -30 | 0.0181 | 0.0104 | 0.0461 | 0.0805 | 0.0637 | 0.1314 | 0.1797 |
| -40 | 0.0127 | 0.0459 | 0.0335 | 0.0620 | 0.0786 | 0.1973 | 0.0264 |
| -50 | 0.0516 | 0.0231 | 0.0386 | 0.0363 | 0.0419 | 0.1381 | 0.3554 |
| -60 | 0.0116 | 0.0259 | 0.0698 | 0.0794 | 0.1671 | 0.1349 | 0.2793 |
| -70 | 0.0350 | 0.0238 | 0.0536 | 0.0869 | 0.1644 | 0.4832 | 0.3818 |

(b) Torque derived from the acceleration and shaft moment of inertia

| $i_{sd} \backslash i_{sq}$ [A] | 10 | 20 | 30 | 40 | 50 | 60 | 70 |
|---|---|---|---|---|---|---|---|
| 0 | 0.0067 | 0.0087 | 0.0177 | 0.0427 | 0.0525 | 0.0424 | 0.0606 |
| -10 | 0.0100 | 0.0054 | 0.0209 | 0.0339 | 0.0262 | 0.0375 | 0.0756 |
| -20 | 0.0214 | 0.0263 | 0.0227 | 0.0348 | 0.0754 | 0.0804 | 0.0974 |
| -30 | 0.0069 | 0.0189 | 0.0458 | 0.0684 | 0.0431 | 0.1023 | 0.0832 |
| -40 | 0.0207 | 0.0392 | 0.1069 | 0.0486 | 0.0775 | 0.0913 | 0.2895 |
| -50 | 0.0117 | 0.0607 | 0.0822 | 0.0931 | 0.1884 | 0.2207 | 0.2028 |
| -60 | 0.0224 | 0.0486 | 0.1075 | 0.0818 | 0.0735 | 0.0624 | 0.2676 |
| -70 | 0.0283 | 0.0407 | 0.0832 | 0.0859 | 0.1579 | 0.1276 | 0.3464 |

Table 4.3: Absolute standard deviation of the torque derived from measurements with four different moment of inertia on the rotor shaft [Nm]

$$\sigma T(i_d, i_q) = \sqrt{\frac{1}{n-1} \sum_{l=1}^{n} (T(i_d, i_q, l) - \overline{T(i_d, i_q)})^2} \tag{4.3}$$

where $(T(i_d, i_q, l) - \overline{T(i_d, i_q)})$ yields the absolute difference between the torque results from when one rotor moment of inertia is mounted on the shaft compared with the average torque results from all four rotor moment of inertia, for one $dq$ current combination. The torques calculated from the acceleration (Table 4.3b) tend to give results which

diverges less than the results calculated from the currents and voltages (Table 4.3a). A probable reason for this is the harmonics in the voltage measurements which the variable switching frequency of the current controller gives rise to. Another observation from Table 4.3 is that the standard deviation tends to increase when the currents – which generally also means the torques – increase. A higher torque gives a higher acceleration, which means that less samples are obtained over one test cycle. A lower amount of samples gives a higher risk for an erroneous average value, and the standard deviation is therefor prone to increase with higher torques.

Another way to measure the divergence of the torque estimations is the *relative* standard deviation, which is the absolute standard deviation divided by the mean torque results (for every current combination) multiplied by 100. The relative deviation is interesting as it gives a measure (in percent) of how much an estimation of the torque can be expected to differ depending on the moment inertia of the rotor shaft. Table 4.4 shows the relative standard deviation for all *dq* current combinations. The relative deviation is more even over the range of the torques compared to the absolute, even if a trend of slightly higher deviation for the highest torques still exists. The average relative standard deviation for the two torque estimation procedures – considering all deviations in table 4.4 – are:

$$\sigma_{ag} = 0.25\%$$
$$\sigma_{rs} = 0.21\%$$

### Comparison between $T_{ag}$ and $T_{rs}$

Figure 4.10 shows the relative difference between the mean motor and generator torque ($T_{ag}^{m}$) when $T_{rs}$ and $T_{ag}$ derive the results. The measurements with the heaviest flywheel (Figure 4.10g and 4.10g) are more consistent than when no fly-wheel is mounted on the rotor axis (Figure 4.10a and 4.10b). As a big moment of inertia limits the mechanical dy-

(a) Torque derived from the currents and voltages for each current combination

| $i_{sd}\backslash i_{sq}$ [A] | 10 | 20 | 30 | 40 | 50 | 60 | 70 |
|---|---|---|---|---|---|---|---|
| 0 | 0.512 | 0.445 | 0.318 | 0.393 | 0.322 | 0.281 | 0.206 |
| -10 | 0.231 | 0.351 | 0.212 | 0.306 | 0.040 | 0.282 | 0.314 |
| -20 | 0.084 | 0.160 | 0.180 | 0.260 | 0.147 | 0.298 | 0.147 |
| -30 | 0.213 | 0.062 | 0.185 | 0.245 | 0.169 | 0.283 | 0.344 |
| -40 | 0.135 | 0.250 | 0.122 | 0.173 | 0.180 | 0.389 | 0.047 |
| -50 | 0.510 | 0.116 | 0.131 | 0.094 | 0.089 | 0.253 | 0.582 |
| -60 | 0.108 | 0.122 | 0.223 | 0.193 | 0.331 | 0.231 | 0.428 |
| -70 | 0.308 | 0.106 | 0.162 | 0.200 | 0.308 | 0.781 | 0.548 |

(b) Torque derived from the acceleration and shaft moment of inertia.

| $i_{sd}\backslash i_{sq}$ [A] | 10 | 20 | 30 | 40 | 50 | 60 | 70 |
|---|---|---|---|---|---|---|---|
| 0 | 0.121 | 0.078 | 0.105 | 0.190 | 0.189 | 0.128 | 0.160 |
| -10 | 0.152 | 0.041 | 0.106 | 0.130 | 0.082 | 0.100 | 0.177 |
| -20 | 0.282 | 0.175 | 0.101 | 0.118 | 0.210 | 0.192 | 0.206 |
| -30 | 0.081 | 0.113 | 0.184 | 0.209 | 0.108 | 0.221 | 0.160 |
| -40 | 0.221 | 0.213 | 0.392 | 0.136 | 0.178 | 0.181 | 0.512 |
| -50 | 0.116 | 0.305 | 0.279 | 0.241 | 0.400 | 0.405 | 0.332 |
| -60 | 0.206 | 0.229 | 0.343 | 0.199 | 0.146 | 0.107 | 0.411 |
| -70 | 0.247 | 0.182 | 0.251 | 0.198 | 0.196 | 0.206 | 0.528 |

Table 4.4: Relative standard deviation of the torque derived from measurements with four different moment of inertia on the rotor shaft [%]

namics of the machine more than a small, more samples are obtained with a heavier flywheel, and the increased consistency of the results is therefor expected.

Another interesting notation is the small positive error that exists when the $q$ currents are small (Figure 4.10b, 4.10d,4.10f and 4.10h). Looking closer on how the flux vary with the $d$ current (Figure 4.10a, 4.10c, 4.10e and 4.10g), this is especially true when the field-weakening current is big. A small $q$ current and a big $d$ current implies that a small error

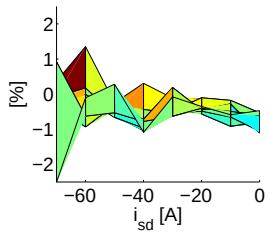


(a) Without flywheel

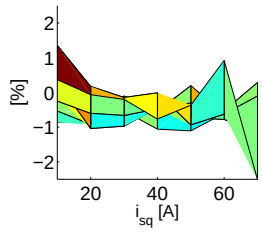


(b) Without flywheel

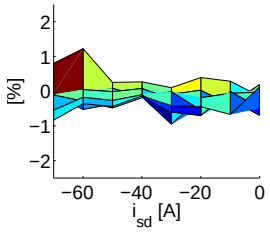


(c) Flywheel number one

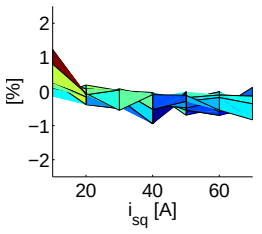


(d) Flywheel number one

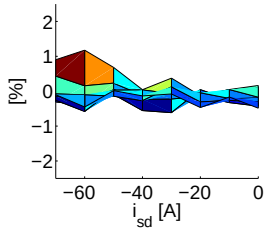


(e) Flywheel number two

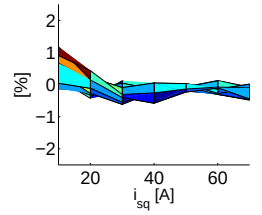


(f) Flywheel number two

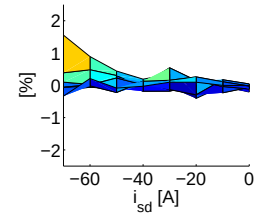


(g) Flywheel number three

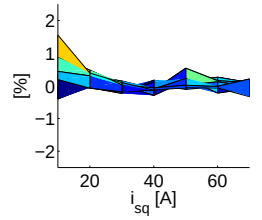


(h) Flywheel number three

Figure 4.10: Difference in measurements between deriving the torque from flux and current and acceleration and moment of inertia. Flywheel one has the least moment of inertia and flywheel three has the most

in the rotor position measurement leads to a relatively big offset in the $q$ current, which has a big influence on the torque. If the flux and the currents derive the results, the post-processing transformations are made with an erroneous angle, and there is consequently an error in the results. The results that the acceleration and moment of inertia give are on the other hand not affected by a offset in the measured angle. $T_{rs}$ therefor gives the true mean torque between the motor and generator operation while $T_{ag}$ gives erroneous results.

An important comment to add to this is that if there is an error in the position estimation, the $dq$ current combination which is actually being evaluated differs from the reference. This means that even if $T_{rs}$ gives the actual torque that is being produced, it is impossible to know which current combination that is tested. The conclusion is that the results presented in Figure 2.11b point towards a small offset in the rotor angle estimation, which imposes a small error in the torque maps. This shows that much attention should be given to the calibration of the rotor position transducer before performing DTM tests.

#### Consecutive measurements with one $dq$ current combination

The last part of the consistency analysis consists of consecutive measurements with specific current combinations to see if the results coincide. Three combinations are chosen for the analysis

1. $i_d$=-10, $i_q$=70
2. $i_d$=-70, $i_q$=70
3. $i_d$=-70, $i_q$=10

Each combination is tested 10 times, whereat the mean value and the standard deviation of $T_{ag}^m$ are calculated for both when $T_{ag}$ and $T_{rs}$ give the results. Furthermore, the tests are conducted both without flywheel and with the heaviest flywheel mounted on the rotor shaft. Table 4.5

(a) Results with no flywheel

| Point | $T_{ag}$ [Nm] | $T_{rs}$ [Nm] |
|---|---|---|
| 1 | $\bar{T} = 42.25, \sigma = 0.09$ | $\bar{T} = 42.36, \sigma = 0.02$ |
| 2 | $\bar{T} = 69.24, \sigma = 0.11$ | $\bar{T} = 68.4, \sigma = 0.03$ |
| 3 | $\bar{T} = 11.38, \sigma = 0.02$ | $\bar{T} = 11.46, \sigma = 0.02$ |

(b) Results with flywheel 3

| Point | $T_{ag}$ [Nm] | $T_{rs}$ [Nm] |
|---|---|---|
| 1 | $\bar{T} = 42.61, \sigma = 0.05$ | $\bar{T} = 42.64, \sigma = 0.02$ |
| 2 | $\bar{T} = 69.28, \sigma = 0.06$ | $\bar{T} = 69.35, \sigma = 0.03$ |
| 3 | $\bar{T} = 11.39, \sigma = 0.01$ | $\bar{T} = 11.53, \sigma = 0.02$ |

Table 4.5: Torque variation in the selected operation points according to measurements

presents the outcome of the experiments.

When no flywheel is mounted on the rotor shaft, $T_{ag}$ gives slightly bigger results than $T_{rs}$, except for in point 3, where the relation is opposite (Table 4.5a). The biggest difference in the torque estimation is in point 2, where the torque – and thus also the acceleration – is highest. It is therefore likely that the difference occur due to very fast mechanical dynamics. This may be due to a slightly too slow low-pass filter when the rotor position measurements are post-processed. A probable reason for the difference in point 3 is, as discussed in the preceding section, a slight offset in the rotor position measurements.

Table 4.5b shows the results from tests when the flywheel is mounted on the shaft. Compared to the results from the tests without a flywheel (Table 4.5a), the standard deviation is consistently lower. This is expected as more samples are obtained when the acceleration is lower. The results from $T_{rs}$ are also consistently bigger in Table 4.5b compared to Table 4.5a, which confirms the suggestion that the lower torque estimations from the experiments without flywheels are due to fast accelerations. The difference in point 3 is still present in the experiments with the flywheel, which further confirms the proposition that the rotor position may be badly calibrated.

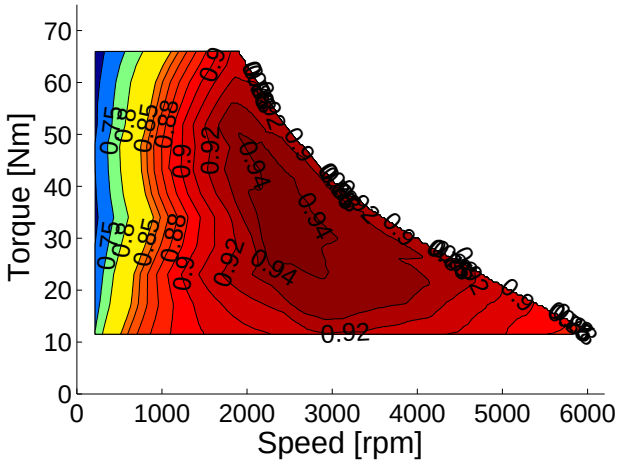


Figure 4.11: Efficiency measurement as a function of speed and torque

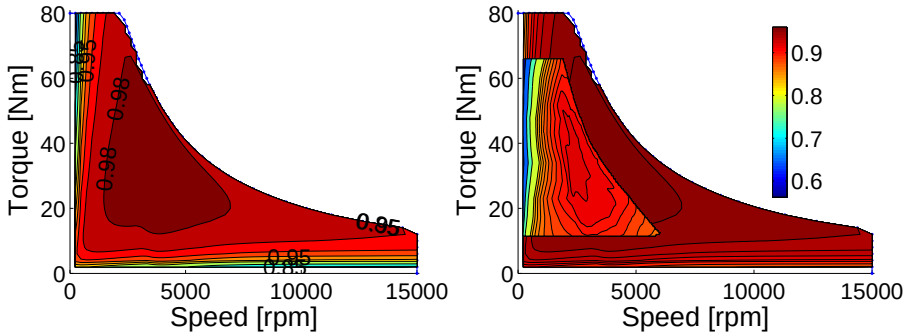


(a) Simulation of efficiency as a function of speed and torque

(b) Comparison between simulated and measured efficiency

Figure 4.12: Simulated efficiency measurements

## 4.3 Efficiency measurements

Figure 4.11 shows the efficiency results of the dynamic measurements. The current combinations that were tested ranges from $i_q = 10 : 60$ A and $i_d = 0 : -80$ A in steps of 10 A. The upper limit for the torque is

65 Nm, and the lower limit is 11 A, which is the range of the torque that the machine produces with the tested current combinations.

The efficiency is low for a low speed and high torque operation due high copper losses. At high speeds, the iron losses increases, and the efficiency consequently decreases. The results show a maximum efficiency of 94 %. The maximum speed of the machine is around 6000 rpm, which seams low, though it should be mentioned that current combinations with lower $q$ current and higher negative $d$ current that is outside of the tested current range might lead to results of higher speed and higher efficiency.

The DC voltage source which was used throughout the experiments also gives an explanation for the low top speed. The source is a DC machine which is connected mechanically to a asynchronous motor, which in turn is connected to the grid. The DC link voltage tend to drop when the speed increases since the test object demands more power (if the torque is constant). The increase in power means that the torque of the asynchronous machine increases, which leads to an increase in the slip. Since the induced voltage in the DC machine is proportional to the rotational speed, the DC link voltage of the converter consequently drops. Since the speed of the test object is limited by the DC voltage, the maximum speed of each current combination drops as well.

To compare the measured efficiency to the machine's expected performance, it was modeled and simulated in the FEMM software. The simulations were conducted with a DC link voltage of 300 V, which is the same voltage that was used in the experiments. Figure 4.12a displays the results from the efficiency simulation and Figure 4.12b shows a comparison between the two results. The simulated maximum speed is around three times higher than the results from the experimental tests, and the maximum efficiency of the simulations is 4 % higher. The efficiency is expected to differ since no mechanical or rotor losses are included in the FEMM model. The big speed difference is on the other hand not expected. Even if the explanations from the previous paragraphs give an idea of what might cause the difference, the divergence still gives room for future research.

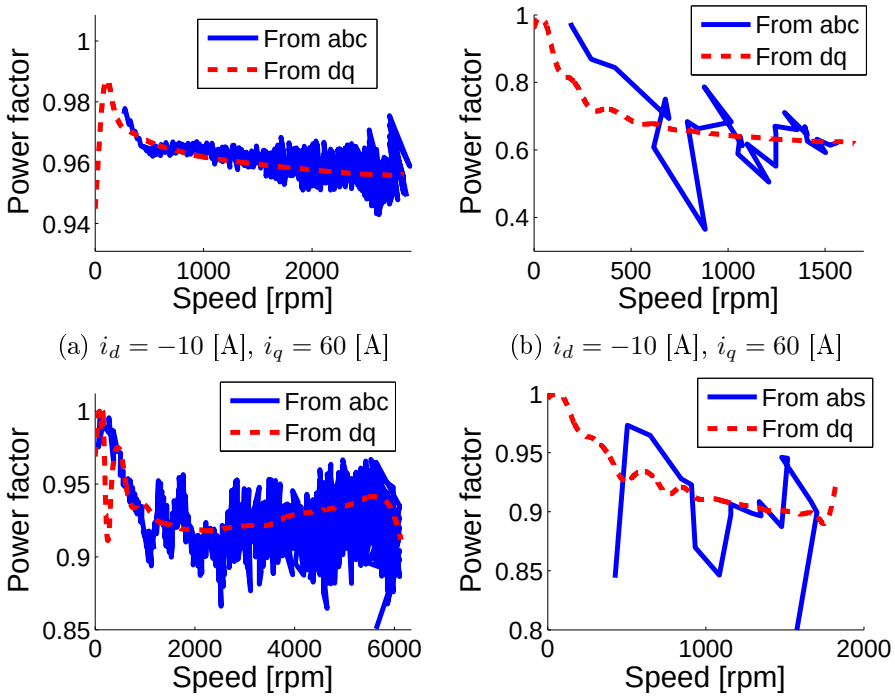


(a) $i_d = -10$ [A], $i_q = 60$ [A]

(b) $i_d = -10$ [A], $i_q = 60$ [A]

(c) $i_d = -80$ [A], $i_q = 60$ [A]

(d) $i_d = -80$ [A], $i_q = 60$ [A]

Figure 4.13: Power factor with different current combinations, derived from both the phase and the $dq$ voltages and currents

## 4.4 Power Factor

Figure 4.13 shows the derived power factor of the machine from both the phase and the $dq$ voltages and currents for four different current combinations. The $dq$ voltages and currents give a result with slow dynamics over the speed range due to the filtered signals. The abc voltage and currents give results with big variations. Since the algorithm which derives the power factor from the abc measurements must iterate through all periods to estimate the local phase shift and frequency, it consumes much more time than the calculations from the $dq$ variables. With this in mind, only results from the $dq$ method of all tested current

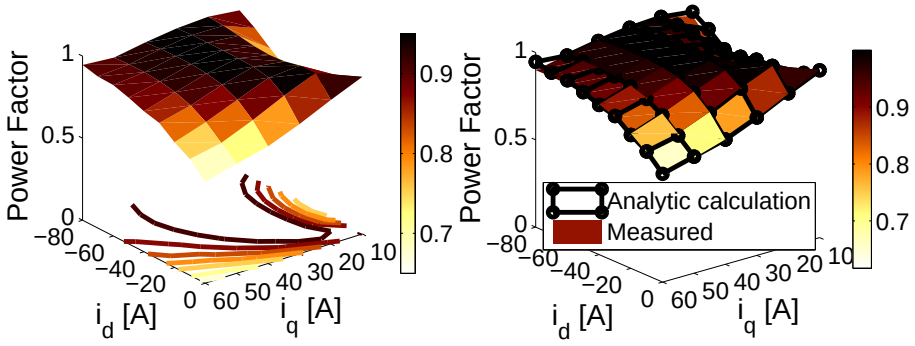


(a) Power factor measurements at 1400 rpm

(b) Comparison between measurements and analytically calculated results

Figure 4.14: Power factor measurements

combinations are presented. Figure 4.14a shows the derived power factor at 1400 rpm.

To control if the measurement results are reasonable, the power factor is also estimated by an analytic function. The easiest way to derive an expression for the power factor is to find the angle between the $dq$ voltages and currents. Supposing that the stator resistance and the linked magnetic flux are known, the $dq$ voltages for a specific current combination can be derived from the PMSM voltage equations. The arcus tangens function gives the angle of the voltage and current vector in relationship to the $d$-axis. Cosinus of the angle between the $dq$ voltage and current vectors gives the power factor.

Figure 4.14b shows a comparison between the measurements and the analytic estimation. The results fits well, but there exists a small difference when the field weakening current is high. The field-weakening current makes the induced voltage relatively small. On the other hand, the big current leads to a big resistive voltage drop. This makes the analytical estimation sensitive to errors in the resistance, which might provide an explanation for the difference between the analytic and the experimental results.

# Chapter 5

# Deeper Analysis of Results

This chapter aims to analyze the obtained results on a deeper level than in chapter 4 to look for unexpected phenomena. A definitive explanation of the findings are out the scope of this thesis; rather, this section presents and discusses possible explanations to the results. First, the flux linkage results as functions of speeds are presented. Secondly, the torque, losses and efficiency are analyzed.

## 5.1 Flux linkage

Figure 5.1 shows the flux as a function of speed from both the magnetic model identification test and the efficiency test. The results present two phenomena which are unexpected: The results from the tests with the field oriented control have an offset between when the machine works as a motor and when it works as a generator; furthermore, the flux from both methods show an considerable speed dependence.

Since the offset is only present from the FOC measurement, a thorough comparison between the two test methods is in order. A big difference between the DCC and the FOC is the variable and constant switching frequency which they feature. A constant switching frequency implies that the frequency of the ripple of the current is constant. This in turn implies that, if the sampling of data is synchronized with the frequency, the control system samples the current on a specific point on the ripple

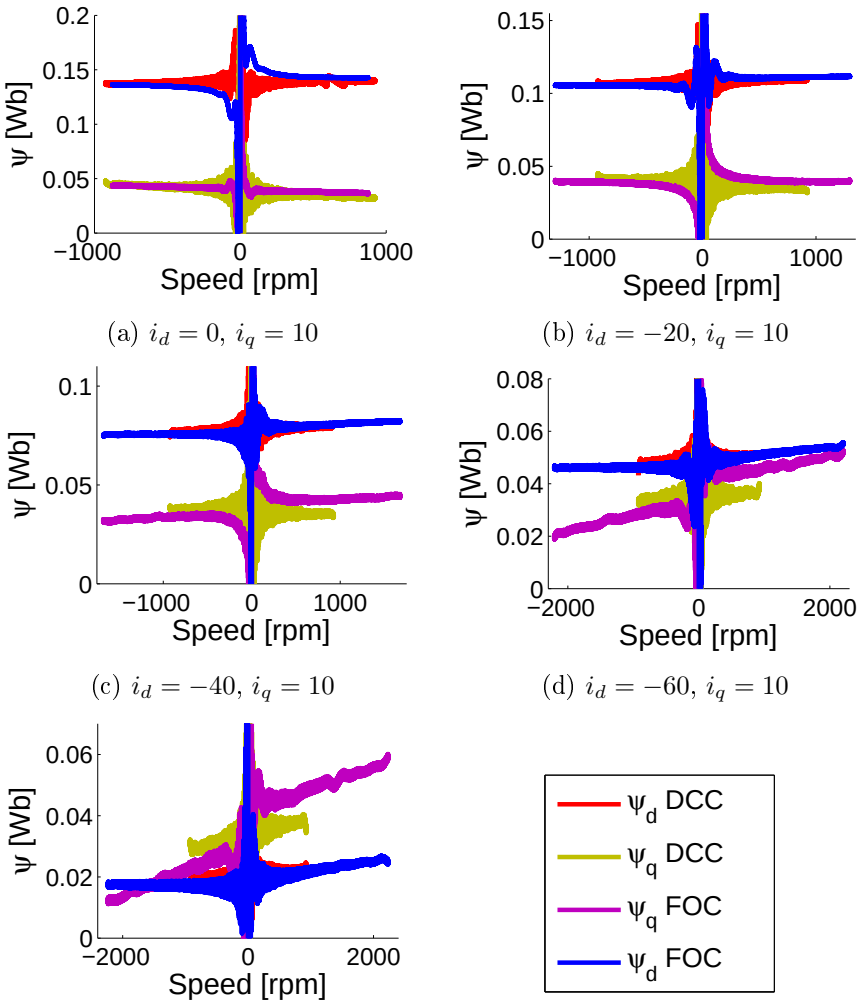


(a) $i_d = 0$, $i_q = 10$

(b) $i_d = -20$, $i_q = 10$

(c) $i_d = -40$, $i_q = 10$

(d) $i_d = -60$, $i_q = 10$

(e) $i_d = -80$, $i_q = 10$

Figure 5.1: Magnetic linked flux as a function of speed over test sequences

each switching period. With a variable frequency, the data sampling is not in synchronization with the switching, and the obtained data is randomized over the current ripple.

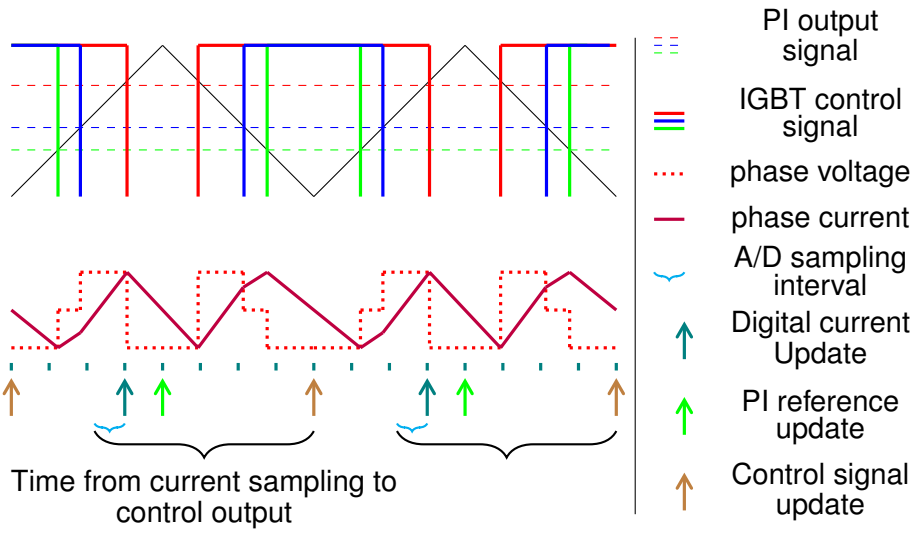


Figure 5.2: Field oriented control signal path in the control system

This work's control system measures the current data eight times every FOC switching period, but updates the current controller reference value only one time per switching period. On top of that, the analog input takes one micro second to convert the measured data to a digital fixed point variable for the control system. Figure 5.2 illustrates the IGBT control signal output pf the system, one resulting converter phase voltage and current, and points in time of sampling. The current signal which works as the input to the current controller is consistently sampled on the active vectors which are applied in the first half of the carrier wave. This leads to an offset in the measured current which may trick the control system to believe that the current is higher or lower than it actually is.

Figure 5.3 shows the phenomenon in the $\alpha\beta$ and the $dq$ plane. Due to the changed direction of the induced voltage when the machine works as a motor compared to when it works as a generator, the control system applies the voltage vectors in a different order. This means that the current ripple is located on different sides of the reference in the $dq$ coordinates when it is sampled (within the dashed circles). When the

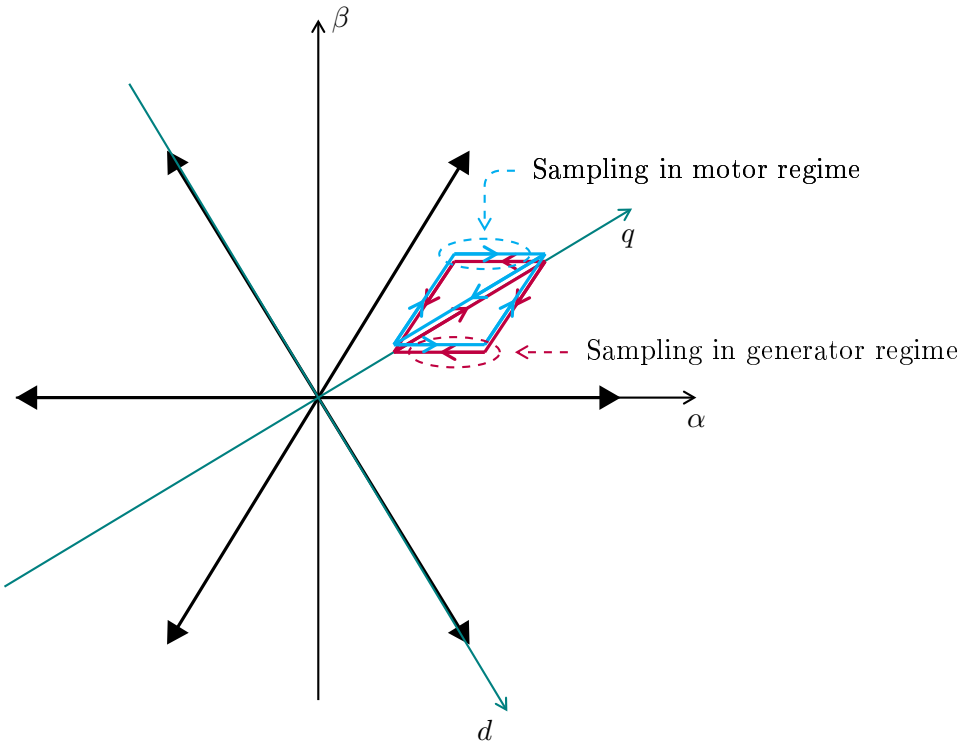


Figure 5.3: Current path in $\alpha\beta$ and $dq$ coordinates. The dashed circles are where the current is sampled for the control system

reference is only in the $q$ direction, as in Figure 5.3, the measured current has a negative offset when the machine works as a motor and vice versa in generator mode. Consequently, the current controller makes the $d$ current positive in motor mode and negative in generator mode, even though its reference is zero. This means that the resulting flux becomes bigger in the motor regime and smaller in generator regime.

Another difference between the two control methods is the ability to produce sinusoidal currents in high field weakening operation. Figure 5.4 shows the currents in $\alpha\beta$ coordinates when different field weakening currents are imposed on the machine. The field weakening introduces significant low frequency harmonics in the FOC compared to the DCC.

Since these currents have a different angular frequency than the rotor, they introduce phenomena such as iron eddy currents and hysteresis loops, which can interfere with the magnetic flux path of the fundamental component of the flux. With this in mind, it is unexpected that the currents does affect the $q$ flux rater than the $d$ flux since the non-laminated permanent magnets are on the $d$ axis. A further analysis on how the harmonics affect the flux requires finite element simulations, and are out the scope of this thesis; with that being said, it is possible that the prominent harmonics can give a clue about why the linkage change between motor and the generator operation of the machine.

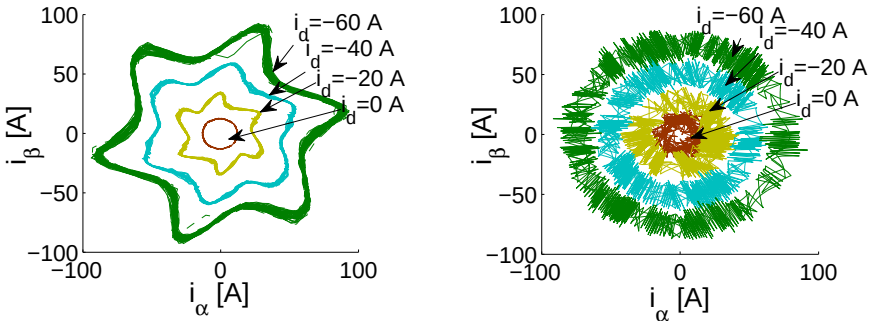


(a) Field oriented control (b) Direct current control

Figure 5.4: $\alpha\beta$ currents when different control methods are used

A third point, which is partly discussed above, is that the switching frequency differs between the DCC and the FOC. As a matter of fact, the average switching frequency of the DCC can be as low as 2000 Hz at low speed operation [59]. A high switching frequency makes the influence of for example the neglected rise and fall times of the power modules much bigger, which gives rise to measurement errors of the voltage. Voltage measurement errors lead directly to a error in the flux derivation. To control if it is the measurement procedure that introduces the unexpected phenomena an additional voltage measurement method can be used, but such measurements are not presented here due to lack of time.

Since both of the control methods are dependent on the speed in a similar way, it is not enough to analyze the control method's influence on

the results. As described chapter 2, the measured voltage – which gives the flux estimation – is measured by integrating one switching period. This means that the mean value after the integration is delayed by half a switching period when the control system obtains it. Furthermore, the integrated value is stored away for post-processing half a switch period after it is obtained. The position, on the other hand, is delayed in between one eight and one quarter of a switching period depending on the timing between the A/D conversion and the sampling of the resolver signal. This means that there exists a time shift between the voltage and position of three quarters to one half of a switching period in the instance that the control system stores the values.

The time shift makes the torque angle value differ as the peak of the voltage vector is shifted slightly in the $dq$ frame. Furthermore, as the frequency of the fundamental period of the voltage increases, the shift in angle increases as well. Since the control system stores the data with two times the converter switching frequency, it is possible to account for the time shift approximately by shifting the voltage vector one sample forward in the post-processing data vector. Figure 5.5 shows a comparison between the flux after and before the synchronization of the data. The synchronization almost completely removes the $d$ flux speed dependence, but enforces the dependence in $q$; it thus seams like the speed dependence of the $q$ flux is due to another phenomenon.

This analysis of the flux results provides some important lessons: The choice of method which controls the current throughout the testing is important, and small details have rather big consequences. Furthermore, the synchronization of data affects the results in a notable way. A shift of 50 microseconds between the voltage and the position has considerable effects – especially when the speed is high. With all this in mind, it should be said that the dynamic test method for flux derivation – as it is presented in this work – is almost completely unaffected by these effects since the average value of the results from the generator and motor operation is used.

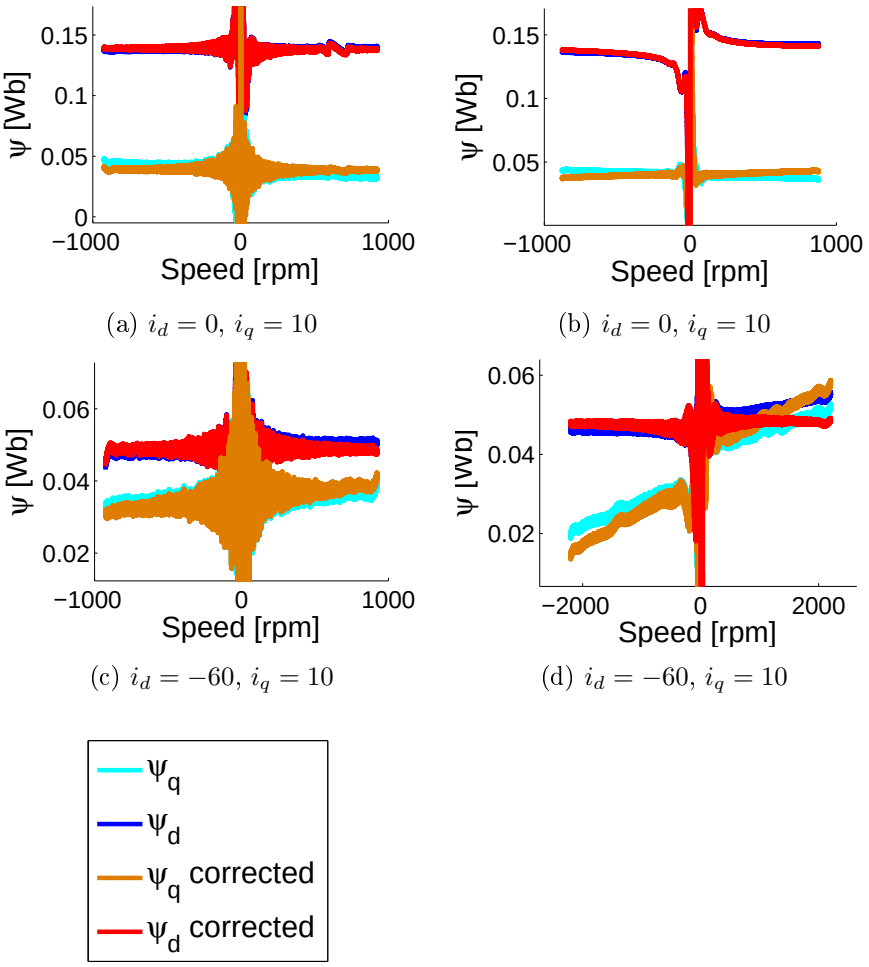


(a) $i_d = 0$, $i_q = 10$

(b) $i_d = 0$, $i_q = 10$

(c) $i_d = -60$, $i_q = 10$

(d) $i_d = -60$, $i_q = 10$

Figure 5.5: Linked magnetic flux with synchronization of samples

## 5.2 Torque and efficiency

Figure 5.6 shows the rotor shaft torque as a function of speed when different field-weakening currents are imposed on the stator windings. As mentioned in chapter 2, the measurements consist of the air-gap torque

and the loss torque, and the loss torque has two speed independent parts – the torque due to iron losses and friction – and one part that is proportional to the speed – the Eddy current losses. It is therefor not surprising that there exists a small offset between the torque when the machine works as a generator and as a motor around zero speed. What is unexpected is the increase or decrease of torque when the machine works as a motor or a generator, respectively; if the air-gap torque is constant, the eddy currents should introduce a small decrease in torque when the machine works as a motor and vice versa.

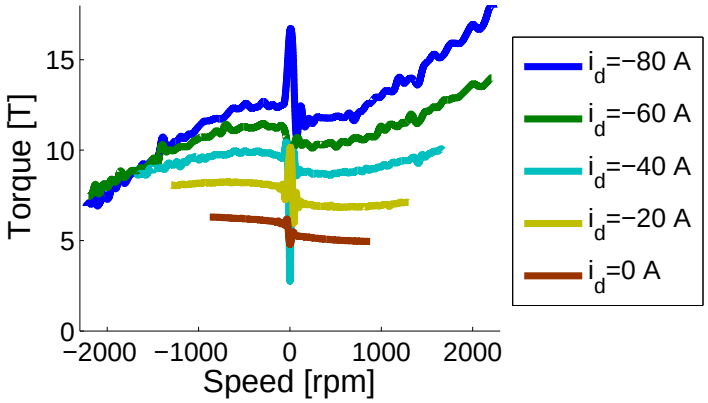


Figure 5.6: Torque with different field weakening currents when $i_q = 10$ A

Figure 5.7 provides an explanation to this phenomenon. The air-gap torque increases with frequency almost exactly with the mechanical torque which explains the behavior in Figure 5.6. This insinuates that the flux dependence on speed which the results from the previous section presents is not a measurement error. On the other hand, the offset between the air-gap and the rotor shaft torque seams unrealistically big. Furthermore, the distance between the air-gap torque and the rotor shaft torque seams to decrease with speed when the field-weakening current is very high (Figure 5.7b). This behavior is very unexpected as it indicates that the loss torque decreases with frequency.

To investigate these phenomena closer, Figure 4.10 shows the difference

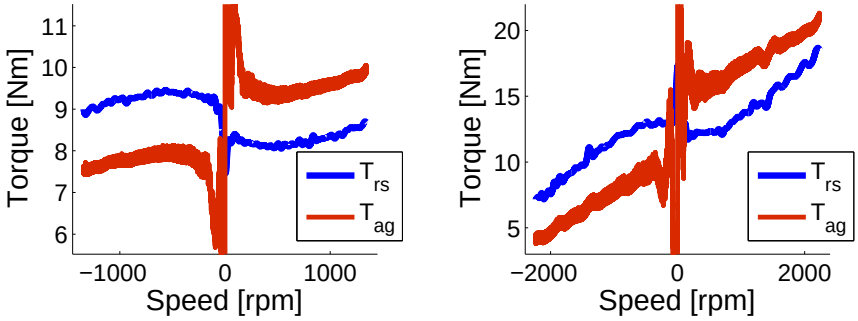


(a) $i_d = -40$, $i_q = 10$ (b) $i_d = -80$, $i_q = 10$

Figure 5.7: Rotor shaft torque and air-gap torque

between the air-gap torque and the rotor shaft torque as a function of speed for a set of current combinations; this is interpreted as the loss torque (in the motor regime, the torque is negative since the the rotor shaft is subtracted by the air-gap torque). All combinations show a big jump in torque as soon as the machine starts spinning, regardless if it works as a motor or a generator. A jump is expected as the friction and hysteresis losses immediately give rise to a loss torque. Even so, the difference is bigger than expected. Even more remarkable is the increase of the difference with field-weakening current when $i_q$ is low; there is no reason to believe that the friction or the hysteresis losses increase when $i_d$ is introduced. Instead, this result insinuates that the big offset in the flux (Figure 5.1) is due to a measurement error rather than an actual physical phenomenon.

When a low $q$ current is imposed on the machine (Figure 5.8a), zero field-weakening current shows a slight increase in the difference between the air-gap and the rotor shaft torque with speed. This is expected as the eddy currents generate more loss with an increased frequency. When $i_d$ is equal to -30 A, the change with speed is zero, and when $i_d$ is increased to -60 A, the difference decreases with frequency. The decrease of difference is very unexpected, and is probably due to a measurement error. One explanation could be that the voltage and position measurement are not in perfect synchronization. Figure 5.5 shows that the

synchronization affects the perceived relationship between the $d$ and $q$ current, which in turn affects the air-gap torque calculation.

When the $q$ current increases (Figure 5.8b), the difference of the torque results oscillate, which makes it hard to appreciate the trend of the losses. This is due to a high torque and a low rotor shaft moment of inertia, which leads to a lot of noise in the position measurements. The high amount of noise makes it hard to find an algorithm which filters away the oscillations but still keeps the position of the fundamental frequency intact. An appropriate filter algorithm for the torque difference should be able to solve this problem since the change of the fundamental of the losses is much slower than the oscillations. Such an algorithm has yet not been developed but is a topic for future research.

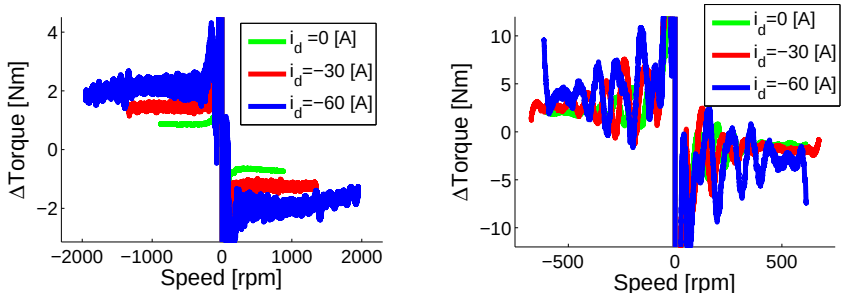


(a) $i_q = 10$ A (b) $i_q = 50$ A

Figure 5.8: Difference between air-gap and rotor shaft torque

The main conclusion of the analysis of the torque measurements is that the DTM needs more development to derive an accurate estimation of the losses in a machine. The offset of the loss torque when the machine goes from zero speed to rotation is unrealistically big, and the change of losses over speed is decreasing with higher frequencies. Both of these phenomena point towards measurement errors. The DAQ system and post-processing algorithm should therefor be refined for a better performance. The big jump in loss torque also provides a likely explanation for the low efficiency which chapter 4 presents. An overestimation of the loss torque correlates directly with a lower efficiency estimation.

# Chapter 6

# Conclusions and Future Work

To round of the Dynamic Test Method (DTM) project, the list below presents items which are worth to take along from this thesis

- The magnetic model identification part of the DTM shows good performance and is ripe to introduce to the industry. The method presents an alternative to the Stand-Still Methods, which are unable to derive the linked flux from the permanent magnets, and to the constant speed methods, which are inefficient in terms of time and cost. It fits perfectly in situations where tests of many machines are necessary – for example, in the end of a production line to double check the performance of the machines. It can also be valuable to provide a first quick feedback to designers when test facilities are hard to come by.

- The efficiency part of the DTM still needs development to produce accurate results. Even so, it shows promise to eventually become a valuable asset for the industry. The method should not be seen as a replacement for the constant speed methods which provide very accurate measurements. Instead, it suits as a compliment which can be used when speed has higher priority than very exact accuracy. This can be extra valuable when test facilities are fully booked and a first quick evaluation is desired.

- There still exist phenomena in the measurements which are left unexplained. If the method is to be extended to include an accu-

rate loss separation, these phenomena must be understood and, in the case of measurement error, be compensated for.

- Supposing an accurate loss separation, the method can be extended to derive the thermal characteristics of the test object. This in turn gives possibilities to develop dynamic drive cycle testing. In addition, the method could be extended to include other machines, such as asynchronous and DC machines; machines which are also used frequently in the vehicle industry.

# References


[1] Ieee guide: Test procedures for synchronous machines. *IEEE Std 115-1995*, pages i–, 1995.

[2] A. Reinap, D. Hagstedt, F. Marquez, Y. Loayza, and M. Alakula. Development of a radial flux machine design environment. In *Electrical Machines, 2008. ICEM 2008. 18th International Conference on*, pages 1–4, Sept 2008.

[3] N. Bianchi and S. Bolognani. Magnetic models of saturated interior permanent magnet motors based on finite element analysis. In *Industry Applications Conference, 1998. Thirty-Third IAS Annual Meeting. The 1998 IEEE*, volume 1, pages 27–34 vol.1, Oct 1998.

[4] M.A. Hamida, J. De Leon, A. Glumineau, and R. Boisliveau. An adaptive interconnected observer for sensorless control of pm synchronous motors with online parameter identification. *Industrial Electronics, IEEE Transactions on*, 60(2):739–748, Feb 2013.

[5] Kan Liu and Z.Q. Zhu. Online estimation of the rotor flux linkage and voltage-source inverter nonlinearity in permanent magnet synchronous machine drives. *Power Electronics, IEEE Transactions on*, 29(1):418–427, Jan 2014.

[6] Kan Liu, Z.Q. Zhu, and D.A. Stone. Parameter estimation for condition monitoring of pmsm stator winding and rotor permanent magnets. *Industrial Electronics, IEEE Transactions on*, 60(12):5902–5913, Dec 2013.

[7] R. Dutta and M.F. Rahman. A comparative analysis of two test

methods of measuring d - and q -axes inductances of interior permanent-magnet machine. *Magnetics, IEEE Transactions on*, 42(11):3712–3718, Nov 2006.

[8] M. Kazerooni, S. Hamidifar, and N.C. Kar. Analytical modelling and parametric sensitivity analysis for the pmsm steady-state performance prediction. *Electric Power Applications, IET*, 7(7):586–596, Aug 2013.

[9] B. Stumberger, G. Stumberger, D. Dolina, A. Hamler, and M. Trlep. Evaluation of saturation and cross-magnetization effects in interior permanent magnet synchronous motor. In *Industry Applications Conference, 2001. Thirty-Sixth IAS Annual Meeting. Conference Record of the 2001 IEEE*, volume 4, pages 2557–2562 vol.4, Sept 2001.

[10] D.M. Saban, D.A. Gonzalez-Lopez, and C. Bailey. Beyond ieee std 115 and api 546: Test procedures for high-speed multimegawatt permanent-magnet synchronous machines. *Industry Applications, IEEE Transactions on*, 46(5):1769–1777, Sept 2010.

[11] H. Karmaker. Report on ieee standard working group p1812 on guide for testing permanent magnet machines. In *Energy Conversion Congress and Exposition (ECCE), 2012 IEEE*, pages 2326–2333, Sept 2012.

[12] H.A. Toliyat and G.B. Kliman. *Handbook of Electric Motors*. Electrical and computer engineering. CRC Press, 2004.

[13] Y. Loayza, A. Reinap, and M. Alakula. Performance and efficiency evaluation of fpga controlled ipmsm under dynamic loading. In *Diagnostics for Electric Machines, Power Electronics Drives (SDEMPED), 2011 IEEE International Symposium on*, pages 550–555, Sept 2011.

[14] V.B. Honsinger. Performance of polyphase permanent magnet ma-

chines. *Power Apparatus and Systems, IEEE Transactions on*, PAS-99(4):1510–1518, July 1980.

[15] A.H. Wijenayake and P.B. Schmidt. Modeling and analysis of permanent magnet synchronous motor by taking saturation and core loss into account. In *Power Electronics and Drive Systems, 1997. Proceedings., 1997 International Conference on*, volume 2, pages 530–534 vol.2, May 1997.

[16] M. Kazerooni, S. Hamidifar, and N.C. Kar. Analytical modelling and parametric sensitivity analysis for the pmsm steady-state performance prediction. *Electric Power Applications, IET*, 7(7):586–596, Aug 2013.

[17] T. Herold, D. Franck, Enno Lange, and K. Hameyer. Extension of a d-q model of a permanent magnet excited synchronous machine by including saturation, cross-coupling and slotting effects. In *Electric Machines Drives Conference (IEMDC), 2011 IEEE International*, pages 1363–1367, May 2011.

[18] A. Gebregergis, M. Chowdhury, M. Islam, and T. Sebastian. Modeling of permanent magnet synchronous machine including torque ripple effects. In *Energy Conversion Congress and Exposition (ECCE), 2013 IEEE*, pages 2108–2114, Sept 2013.

[19] Bong-Hwan Kwon, Byung-Duk Min, and Jang-Hyoun Youm. An improved space-vector-based hysteresis current controller. *Industrial Electronics, IEEE Transactions on*, 45(5):752–760, Oct 1998.

[20] M. Mohseni, S.M. Islam, and M.A.S. Masoum. Enhanced hysteresis-based current regulators in vector control of dfig wind turbines. *Power Electronics, IEEE Transactions on*, 26(1):223–234, Jan 2011.

[21] M. Mohseni and S.M. Islam. A new vector-based hysteresis current control scheme for three-phase pwm voltage-source inverters.

*Power Electronics, IEEE Transactions on*, 25(9):2299–2309, Sept 2010.

[22] A. Tilli and A. Tonielli. Sequential design of hysteresis current controller for three-phase inverter. *Industrial Electronics, IEEE Transactions on*, 45(5):771–781, Oct 1998.

[23] J.A. Suul, K. Ljokelsoy, T. Midtsund, and T. Undeland. Synchronous reference frame hysteresis current control for grid converter applications. *Industry Applications, IEEE Transactions on*, 47(5):2183–2194, Sept 2011.

[24] M.-W. Naouar, A.A. Naassani, E. Monmasson, and I. Slama-Belkhodja. Fpga design for direct sliding mode current control of a synchronous machine. In *Applied Power Electronics Conference and Exposition, 2009. APEC 2009. Twenty-Fourth Annual IEEE*, pages 204–209, Feb 2009.

[25] S. Adhikari N. A. J. Lieven. Error analysis in trifilar inertia measurements. *Experimental Mechanics*, 135(4):533–540, August 2009.

[26] N.P.Quang and J.-A.Dittrich. *Vector control of Three-Phase AC machines: System Development in the Practice.* Springer-Verlag Berlin Heidelberg, 2008.

[27] Lennart Harnefors and H.-P. Nee. Model-based current control of ac machines using the internal model control method. *Industry Applications, IEEE Transactions on*, 34(1):133–141, Jan 1998.

[28] A. Boglietti, P. Ferraris, M. Lazzari, and M. Pastorelli. Change of the iron losses with the switching supply frequency in soft magnetic materials supplied by pwm inverter. *Magnetics, IEEE Transactions on*, 31(6):4250–4252, Nov 1995.

[29] M. Nasir Uddin and HongBin Zou. Comparison of dtfc and vector control techniques for pmsm drive with loss minimization ap-

proach. In *Electrical and Computer Engineering (CCECE), 2014 IEEE 27th Canadian Conference on*, pages 1–5, May 2014.

[30] A. Krings, J. Soulard, and O. Wallmark. Pwm influence on the iron losses and characteristics of a slotless permanent-magnet motor with sife and nife stator cores. *Industry Applications, IEEE Transactions on*, 51(2):1475–1484, March 2015.

[31] T.M. Jahns, G.B. Kliman, and Thomas W. Neumann. Interior permanent-magnet synchronous motors for adjustable-speed drives. *Industry Applications, IEEE Transactions on*, IA-22(4):738–747, July 1986.

[32] Y.A.-R.I. Mohamed and T.K. Lee. Adaptive self-tuning mtpa vector controller for ipmsm drive system. *Energy Conversion, IEEE Transactions on*, 21(3):636–644, Sept 2006.

[33] Sungmin Kim, Young-Doo Yoon, Seung-Ki Sul, and K. Ide. Maximum torque per ampere (mtpa) control of an ipm machine based on signal injection considering inductance saturation. *Power Electronics, IEEE Transactions on*, 28(1):488–497, Jan 2013.

[34] S. Morimoto, Y. Tong, Y. Takeda, and T. Hirasa. Loss minimization control of permanent magnet synchronous motor drives. *Industrial Electronics, IEEE Transactions on*, 41(5):511–517, Oct 1994.

[35] A. Rabiei, T. Thiringer, and J. Lindberg. Maximizing the energy efficiency of a pmsm for vehicular applications using an iron loss accounting optimization based on nonlinear programming. In *Electrical Machines (ICEM), 2012 XXth International Conference on*, pages 1001–1007, Sept 2012.

[36] Ronggang Ni, Dianguo Xu, Gaolin Wang, Li Ding, Guoqiang Zhang, and Lizhi Qu. Maximum efficiency per ampere control of permanent-magnet synchronous machines. *Industrial Electronics, IEEE Transactions on*, 62(4):2135–2143, April 2015.

[37] Giorgio Bertotti. General properties of power losses in soft ferromagnetic materials. *Magnetics, IEEE Transactions on*, 24(1):621–630, Jan 1988.

[38] R. Ramakrishnan, A. Gebregergis, M. Islam, and T. Sebastian. Effect of position sensor error on the performance of pmsm drives for low torque ripple applications. In *Electric Machines Drives Conference (IEMDC), 2013 IEEE International*, pages 1166–1173, May 2013.

[39] S. Sarma, V.K. Agrawal, and S. Udupa. Software-based resolver-to-digital conversion using a dsp. *Industrial Electronics, IEEE Transactions on*, 55(1):371–379, Jan 2008.

[40] D.A. Khaburi. Software-based resolver-to-digital converter for dsp-based drives using an improved angle-tracking observer. *Instrumentation and Measurement, IEEE Transactions on*, 61(4):922–929, April 2012.

[41] Jack E. Volder. The cordic trigonometric computing technique. *Electronic Computers, IRE Transactions on*, EC-8(3):330–334, Sept 1959.

[42] D. Hanselman. Resolver signal requirements for high accuracy resolver-to-digital conversion. In *Industrial Electronics Society, 1989. IECON '89., 15th Annual Conference of IEEE*, pages 486–493 vol.2, Nov 1989.

[43] D.C. Hanselman. Techniques for improving resolver-to-digital conversion accuracy. *Industrial Electronics, IEEE Transactions on*, 38(6):501–504, Dec 1991.

[44] N.L.H. Aung, c. bi, A. Al Mamun, C.S. Soh, and Y. YinQuan. A demodulation technique for spindle rotor position detection with resolver. *Magnetics, IEEE Transactions on*, 49(6):2614–2619, June 2013.

[45] T.-H. Chin, Motomu Nakano, and T. Hirayama. Accurate measurement of instantaneous voltage for power electronics circuits. In *Power Conversion Conference - Nagaoka 1997., Proceedings of the*, volume 2, pages 881–884 vol.2, Aug 1997.

[46] T.-H. Chin, Motomu Nakano, and T. Hirayama. Accurate measurement of instantaneous values of voltage, current and power for power electronics circuits. In *Power Electronics Specialists Conference, 1998. PESC 98 Record. 29th Annual IEEE*, volume 1, pages 302–307 vol.1, May 1998.

[47] T.D. Batzel and Mihai Comanescu. Instantaneous voltage measurement in pwm voltage source inverters. In *Electrical Machines and Power Electronics, 2007. ACEMP '07. International Aegean Conference on*, pages 168–173, Sept 2007.

[48] L. Peretti and M. Zigliotto. Fpga-based voltage measurements in ac drives. In *Electrical Machines (ICEM), 2010 XIX International Conference on*, pages 1–6, Sept 2010.

[49] Jong-Woo Choi and Seung-Ki Sul. Inverter output voltage synthesis using novel dead time compensation. *Power Electronics, IEEE Transactions on*, 11(2):221–227, Mar 1996.

[50] A.R. Munoz and T.A. Lipo. On-line dead-time compensation technique for open-loop pwm-vsi drives. *Power Electronics, IEEE Transactions on*, 14(4):683–689, Jul 1999.

[51] Sam-Young Kim, Wootaik Lee, Min-Sik Rho, and Seung-Yub Park. Effective dead-time compensation using a simple vectorial disturbance estimator in pmsm drives. *Industrial Electronics, IEEE Transactions on*, 57(5):1609–1614, May 2010.

[52] E. Armando, R.I. Bojoi, P. Guglielmi, G. Pellegrino, and M. Pastorelli. Experimental identification of the magnetic model of synchronous machines. *Industry Applications, IEEE Transactions on*, 49(5):2116–2125, Sept 2013.

[53] Ieee master test guide for electrical measurements in power circuits. *ANSI/IEEE Std 120-1989*, pages 1–125, Nov 1989.

[54] Myoungho Kim, Seung-Ki Sul, and Junggi Lee. Compensation of current measurement error for current-controlled pmsm drives. In *Energy Conversion Congress and Exposition (ECCE), 2012 IEEE*, pages 487–494, Sept 2012.

[55] Francisco Marquez. *Electric Traction Machine Design for an E-RWD Unit*. PhD thesis, Lund University, 2014.

[56] Zhe Huang. Thermal design of electrical machines - investigation and evaluation of cooling performances, 2013. Licentiate Thesis.

[57] Rasmus Andersson. Electric traction machine design for heavy hybrid vehicles, 2014. Licentiate Thesis.

[58] Colonel Wm. T. McLyman. *Transformer and inductor design handbook*. CRC Press, 2011.

[59] S. Hall and Y. Loayza. An evaluation of two direct current control methods implemented with labview on a fpga. In *Electrical Machines and Systems (ICEMS), 2013 International Conference on*, pages 1455–1460, Oct 2013.